MASTER'S THESIS

Characterization of Active Regions for InP-Based MEMS-VCSELs

Erik Haglund

Department of Microtechnology and Nanoscience
CHALMERS UNIVERSITY OF TECHNOLOGY

Walter Schottky Institut
TECHNISCHE UNIVERSITÄT MÜNCHEN

Göteborg/München June 2010

Characterization of Active Regions for InP-Based MEMS-VCSELs

Master's Thesis in Microtechnology and Nanoscience

ERIK HAGLUND, 2010
contact: erik.j.haglund@gmail.com

Department of Microtechnology and Nanoscience
Photonics Laboratory
CHALMERS UNIVERSITY OF TECHNOLOGY
SE-412 96 Göteborg
Sweden
Telephone +46-(0)31-772 1000

Walter Schottky Institut
Chair of Semiconductor Technology
TECHNISCHE UNIVERSITÄT MÜNCHEN
Am Coulombwall 3
D-85748 Garching
Germany
Telephone +49-(0)89-289 12781

Printed at Chalmers Reproservice
Göteborg, Sweden 2010

Abstract

Widely tunable MEMS-VCSELs with a tuning range exceeding 50 nm are currently being developed for applications in reconfigurable optical networks and sensor systems. The tuning range of MEMS-VCSELs is today mainly limited by the width and magnitude of the gain spectra. In order to design new devices with improved performance, especially improved tuning range, detailed knowledge of the gain properties is required. Due to the difficulties associated with performing reliable gain spectra simulations, this thesis is concerned with implementing an experimental procedure to determine the gain characteristics of an active region.

An MBE-grown active region with two AlGaInAs quantum wells was characterized. The gain spectra of the active region was determined by measuring the ASE-spectra and using the Hakki-Paoli method to compute the gain [1]. Care was taken to reduce the influence of the OSA limited linewidth. The Hakki-Paoli method can not be applied directly on a VCSEL, due to its very long free spectral range. The active region was therefore characterized by measurements on edge-emitting Metal-Clad Ridge-Waveguide (MCRW) laser diodes. The lasers had ridge widths of 2-30 μm and lengths of 300-1500 μm. The laser wavelength was 1.5 μm. Due to the lack of lateral current confinement underneath the ridge, the lasers showed a lateral carrier diffusion with almost 20% of the injected current flowing outside of the ridge at threshold for 5 μm wide ridges.

To be able to predict the VCSEL gain from the gain measured in the MCRW lasers, the empirical material gain parameter g_0 was calculated from the measurements. Only the relevant fundamental TE mode was measured by coupling the light into the OSA using a small-aperture polarization maintaining fiber with an in-fiber polarizer. The influence of the current density and heatsink temperature on the gain peak wavelength, FWHM and gain magnitude was investigated.

A g_0=1441 cm^{-1} was measured at 15^{o}C. The peak gain was red-shifted with 0.77 nm/K, and blue shifted with 0.91 nm/mA. The peak net gain was found to decrease with 0.49 cm^{-1}/K.

Keywords: gain spectra measurement, Hakki-Paoli method, Metal-Clad Ridge-Waveguide laser, lateral carrier diffusion, tunable VCSEL, MEMS-VCSEL.

Preface and Acknowledgements

This work was carried out at the Walter Schottky Institut for fundamental research in semiconductor electronics at the Technische Universität München.

I would like to thank Professor Markus-Christian Amann at the Walter Schottky Institut for making this thesis possible and Professor Anders Larsson at the Department of Microtechnology and Nanoscience at Chalmers University of Technology for supporting me throughout this work. My gratitude goes to my supervisors Tobias Gründl and Christian Grasse, who have proven to be fantastic guides on a sometimes rough journey. For valuable discussions about both processing and measurement, I would also like to thank Simeon Katz, Augustinas and Kristijonas Vizbaras, Michael Müller, Arafin Shamsul and Alexander Bachmann.

I am very grateful for the warm welcome I got and great atmosphere among all the people of group E26 at the Walter Schottky Institut. I thank you all for making my stay here a fond memory.

Finally I am grateful for the support from my family and my fellow students at the Engineering Physics programme at Chalmers University of Technology, without whom I would never have made it to this point nor had so much fun during the last six years.

Erik Haglund, München June 2010

Contents

Chapter 1

Introduction

The astonishing development of the World Wide Web during the last one and a half decade, changing the very foundations of our society, would not have been possible without high-speed fiber-optic communication. The use of low-loss optical fibers enables reliable transmission of huge amounts of data at very low costs. Predictions expect a continued strong growth in bandwidth demand, mainly originating from media streaming, see figure 1.1. Examples of such are IPTV (tv over Internet Protocol) and video on demand services with steadily improving picture quality [2].

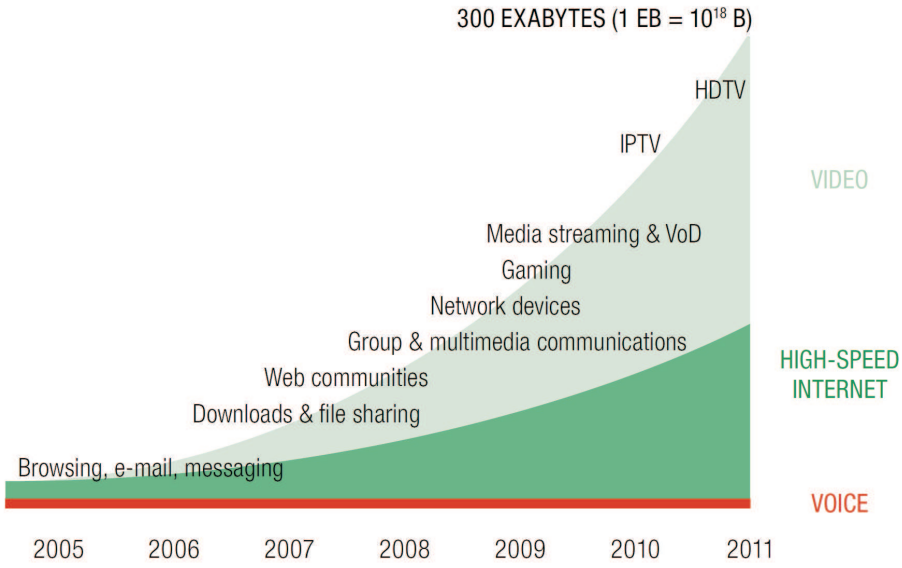

Figure 1.1: Present and predicted annual data traffic for different services.[2]

In order to reach higher data capacity, an even larger portion of the data communication has to be transported and routed in the optical rather than the electrical domain. Fibers going all the way to the end-users are currently being investigated within the concept of Fiber To The Home (FTTH). Even if more data would be transmitted wireless to the end-user, the transmission of data between the network nodes will require more powerful optical solutions. This

includes development of new hardware such as transmitters (lasers), optical passive and active routing, amplifiers and receivers (optical detectors), as well as more efficient modulation formats and signal processing.

The most important candidate for future transmitters in optical networks is the Vertical-Cavity Surface-Emitting Laser (VCSEL), already extensively used in short-range optical communication systems. It has since the first room temperature continuous-wave demonstration in the late 1980's [3] attracted a large interest for applications in optical communication and sensor systems. The possibility of on-chip testing during fabrication, stable single-mode output and high-speed direct modulation as well as high fiber coupling efficiency and simple array integration are advantages of VCSELs compared to other laser designs [4].

Tunable VCSELs, called Micro-Electro-Mechanical System (MEMS) VCSELs, capable of tuning the wavelength over several tens of nanometers, are currently being developed within the EU-project SUBTUNE [5]. The project concerns development of devices covering the wavelength range from 750-2100 nm, with a device tuning range of 60 nm. These can be designed by using different material systems. Lasers covering 1300-2100 nm are made out of the AlGaInAs material system grown on InP wafers. This thesis is focused on InP-based 1550 nm lasers. Major applications of tunable VCSELs in this wavelength range are [5]

- **Transmitters for reconfigurable optical networks and interconnects:** The ability to switch wavelength enables more versatile communication systems, within for instance a Wavelength Division Multiplexing (WDM) system, where several channels at different wavelengths are sent over one fiber. Together with wavelength-selective add/drop multiplexers and optical switches, the development of widely tunable lasers is a large step towards a fully optical network, where a larger part of the signal routing is done in the optical domain. Optical signal processing has the potential of reaching processing speeds 100-1000 times faster than conventional electrical signal processing [2].
- **Sources for fiber Bragg grating sensors:** By utilizing the dispersive properties of a fiber Bragg grating, temperature, pressure and strain can be sensed using a tunable laser.
- **Sources for gas absorption spectroscopy:** The gasses CO, CO_2, NH_3, C_2H_2 and HI (hydrogen iodide) can be detected within the 1.52-1.58 μm range.

Motivation

In order to improve the performance of InP-based tunable VCSELs, advanced simulations to improve the laser design are necessary. A VCSEL is a very complex optical and electrical device, meaning that detailed knowledge of a wide range of different properties, as well as their interaction, is necessary in order to perform these simulations. For tunable VCSELs this gets even more complicated as the spectral dependency of important properties must be taken into account over an extra wide spectral range. The knowledge of the optical gain in these VCSELs is today inadequate. Due to the complicated interaction of many factors affecting the optical gain, realistic gain simulations are difficult. An experimental approach

is therefore preferred to determine the gain characteristics of a certain active region design.

The aim of this thesis is to establish a process and measurement procedure to characterize the gain properties of active regions developed for InP-based MEMS-VCSELs at the Walter Schottky Institut of the Technische Universität München. With a better understanding of the gain properties, improved active regions can be designed.

Thesis Outline

This thesis is concerned with processing and characterization of InP-based lasers with emphasis on the gain properties. The gain spectra can be calculated from the measured Amplified Spontaneous Emission (ASE) spectrum of the laser using a method developed by Hakki and Paoli in the mid 1970's [1]. Necessary theory for measurements and discussions of the gain spectra measurements will be described in chapter 2, 4 and 7.

Direct measurement of the gain spectrum on a VCSEL is not possible due to its large free spectral range. The active region was instead characterized by processing samples into edge-emitting Metal-Clad Ridge-Waveguide (MCRW) lasers, see figure 1.2. The MCRW process is described in chapter 5. The active regions were characterized by measuring the PI- and UI-curves, described in chapter 6, and the ASE-spectra below threshold as discussed in chapter 7. The results will be presented and discussed in chapter 6 and chapter 8.

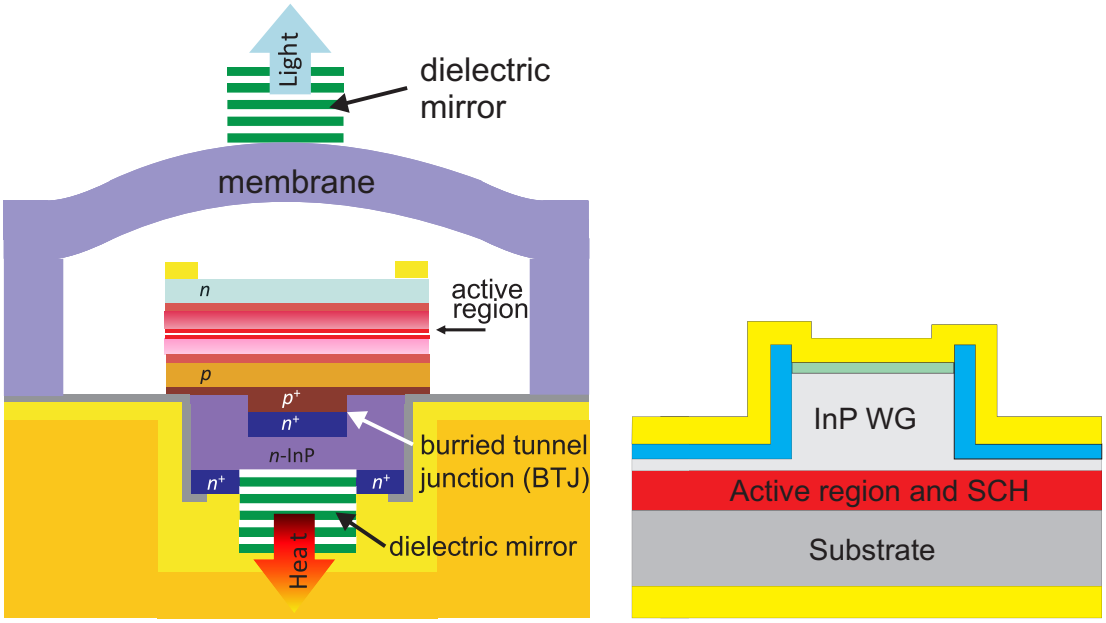

(a) MEMS-VCSEL with an actuatable membrane for tuning.

(b) MCRW laser emitting light out of the plane of the paper.

Figure 1.2: Schematic figures of a MEMS-VCSEL and MCRW laser.

Chapter 2

Laser Theory

Some of the most important equations governing the laser spectrum and behavior will be presented in this chapter. These equations will lead to the equation derived by Hakki-Paoli to calculate the net gain spectrum from the measured ASE-spectrum. In depth treatment of semiconductor lasers can be found in any of many textbooks, for instance [6]. A laser is basically an oscillator working at optical frequencies. Two aligned mirrors forms a cavity, see figure 2.1. By introducing a medium exhibiting optical gain G between the mirrors and pumping it to achieve gain, a resonator is formed.

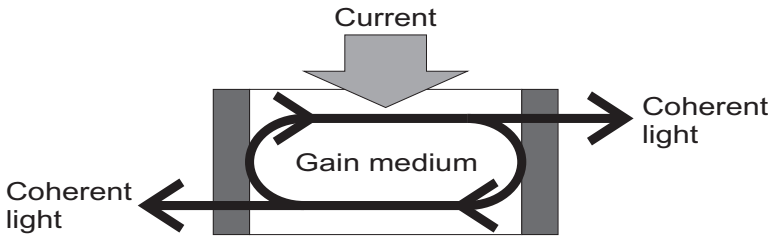

Figure 2.1: Schematic picture of diode laser pumped by an electrical current.

2.1 Fabry-Perot Resonator

An optical cavity formed by two opposing plane mirrors is called a Fabry-Perot (FP) cavity. The mirror reflectivities are denoted r_1 and r_2 for the left and right mirror respectively. The mirror (power) reflectances R_1 and R_2 are simply the squared absolute values of the reflectivities. The general expression for the optical intensity inside a Fabry-Perot cavity can be derived using a plane wave model, see figure 2.2. It is governed by the simple properties of reflection and propagation of electromagnetic fields, as well as the principle of superposition.

Spontaneously emitted photons give rise to an optical field of strength $\overleftarrow{E}_1$ impinging on the first facet, with the arrow indicating the field propagation direction. The resulting reflected field strength is

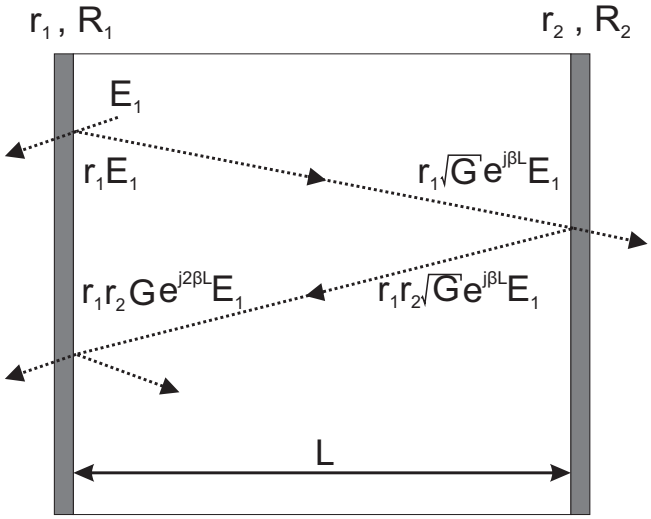

Figure 2.2: Plane wave model of a Fabry-Perot resonator.

$$\overrightarrow{E}_1 = r_1 \overleftarrow{E}_1 \tag{2.1}$$

Assuming that the media between the mirrors is homogeneous with an optical gain per unit length g and loss α_i, the field experiences the linear gain $\sqrt{G} = \sqrt{e^{(g-\alpha_i)L}}$ and a phase shift of $\beta L = 2\pi L n_g/\lambda$ when propagating across the cavity of length L. The n_g is the effective group index of the semiconductor. The field incident on the second facet will be

$$\overrightarrow{E}_2 = \sqrt{G} e^{j\beta L} \overrightarrow{E}_1 = r_1 \sqrt{G} e^{j\beta L} \overleftarrow{E}_1 \tag{2.2}$$

This field is reflected at the second facet with the reflectivity r_2 and propagates back to the first facet, giving

$$\overleftarrow{E}_3 = r_2 \sqrt{G} e^{j\beta L} \overrightarrow{E}_2 = r_1 r_2 G e^{2j\beta L} \overleftarrow{E}_1 \tag{2.3}$$

Thus for every cavity roundtrip the field is multiplied by a factor of $r_1 r_2 G e^{2j\beta L}$. To get the total field impinging on the first facet, all these components must be added

$$\begin{aligned} \overleftarrow{E}_{tot} &= \overleftarrow{E}_1 + \overleftarrow{E}_3 + \overleftarrow{E}_5 + ... \\ &= \overleftarrow{E}_1 + \left(r_1 r_2 G e^{2j\beta L}\right) \overleftarrow{E}_1 + \left(r_1 r_2 G e^{2j\beta L}\right)^2 \overleftarrow{E}_1 + ... \\ &= \sum_{m=0}^{\infty} \left(r_1 r_2 G e^{2j\beta L}\right)^m \overleftarrow{E}_1 \end{aligned} \tag{2.4}$$

This is the sum of a geometric series, which converges for $|x| < 1$ according to

$$\sum_{m=0}^{\infty} x^m = \frac{1}{1-x} \ , \ |x| < 1 \tag{2.5}$$

This gives the total field impinging on the first facet

$$\overleftarrow{E}_{tot} = \frac{\overleftarrow{E}_0}{1 - r_1 r_2 G e^{2j\beta L}} \tag{2.6}$$

It is important to note that this equation was derived assuming that

$$|r_1 r_2 G| < 1 \tag{2.7}$$

This implies that this derivation is only valid below the lasing threshold. The incident optical intensity on the first facet can now be calculated as

$$\begin{aligned} \overleftarrow{I}_{tot}(\lambda) = const \cdot |\overleftarrow{E}_{tot}|^2 &= \frac{\overleftarrow{I}_0}{|1 - r_1 r_2 G e^{2j\beta L}|^2} \\ &= ... \\ &= \frac{\overleftarrow{I}_0}{(1 - r_1 r_2 G)^2 + 4 r_1 r_2 G \sin^2(\beta L)} \end{aligned} \tag{2.8}$$

In the derivation of the equation above, a starting optical field $\overleftarrow{E}_1$ was assumed. This starting field has its origins in spontaneous emission. Since the spontaneous emissions are distributed over the entire cavity length, some photons are amplified and reflected before arriving at the starting position where $\overleftarrow{E}_1$ was defined. By taking this into account, the correct expression for equation 2.8 is [7]

$$\overleftarrow{I}_{tot}(\lambda) = \frac{\overleftarrow{I}_0 (1 + r_1 r_2 G)}{(1 - r_1 r_2 G)^2 + 4 r_1 r_2 G \sin^2(\beta L)} \tag{2.9}$$

Equation 2.9 is schemtically depicted in figure 2.3. Due to destructive and constructive interference of the standing wave inside the Fabry-Perot cavity, the spectrum of the optical field inside the cavity consists of a number of peaks. At wavelengths where the sine factor in equation 2.9 equals zero the intensity inside the cavity will have a maximum, shown as a peak in figure 2.3, while when the sine factor equals one, a minimum is obtained.

To further analyze this spectrum, the roundtrip phase shift can be rewritten as

$$2\beta L = \frac{2\pi\lambda}{(\lambda^2 / 2 L n_g)} = \frac{2\pi\lambda}{\Delta\lambda_{FSR}} \tag{2.10}$$

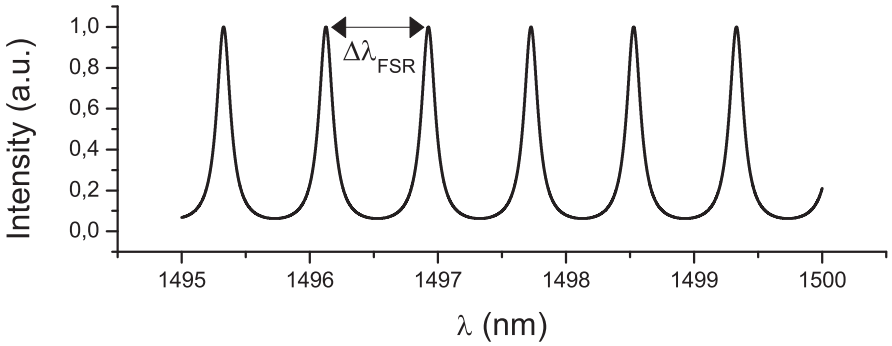

Figure 2.3: Normalized optical intensity inside a Fabry-Perot resonator.

where λ is the free-space wavelength of the optical field and

$$\Delta\lambda_{FSR} = \lambda^2/(2Ln_g) \tag{2.11}$$

is called the Free Spectral Range (FSR) of the cavity and is also the distance between the peaks in the spectrum, see figure 2.3.

2.2 Laser Equations

From the equations previously derived in this chapter, some important basic laser equations can be pointed out. In order to have a stable laser resonator, the optical field must repeat itself after every roundtrip during lasing. This implies that the roundtrip gain must exactly equal the roundtrip losses and the roundtrip phase must equal an even number of π radians. From the roundtrip factor in equation 2.3 this resonator condition is stated in intensity as

$$\left|r_1 r_2 G e^{2j\beta L}\right|^2 = R_1 R_2 e^{2L(\Gamma g_{th} - \alpha_i)} = 1 \tag{2.12}$$

During lasing, the gain clamps to the threshold gain g_{th}. In order to fulfill the above equation it cannot increase any more. In the previous derivation a homogenous medium with gain g was assumed. A semiconductor laser also needs waveguiding, where the light is guided by a high refractive index material surrounded by material with lower refractive index. This means that only a small fraction Γ, called the confinement factor, of the optical field propagates through material experiencing gain. The confinement factor can be calculated by solving Maxwell's equations for the electromagnetic field to satisfy the boundary conditions of the waveguide [10].

It is common to distribute the mirror losses over the cavity length, resulting in a different version of equation 2.12

$$\Gamma g_{th} - \alpha_i = \alpha_m \quad \text{where} \quad \alpha_m = \frac{1}{2L}\ln\left(\frac{1}{R_1 R_2}\right) \tag{2.13}$$

where α_m is called the mirror losses and $\Gamma g - \alpha_i$ is referred to as the net gain. The phase condition is obtained by requiring the roundtrip phase to amount to an even number of π

$$2\beta L = 2m\pi \quad \rightarrow \quad \nu_m = \frac{mc}{2L} = m\Delta\nu_{FSR} \tag{2.14}$$

where ν is the frequency, $\Delta\nu_{FSR}$ is the free spectral range in frequency and the index m designates the m^{th} longitudinal mode of the cavity. It is important to note that the equation $\lambda_m = m\Delta\lambda_{FSR}$ is slightly wrong, as the wavelength according to equation 2.14 *increases* with larger L. This is pointed out here to avoid confusion in the next chapter. In wavelength the correct equation would be

$$\lambda_m = \frac{2Ln_g}{m} = \frac{\lambda_0^2}{m\Delta\lambda_{FSR}} \tag{2.15}$$

where λ_0 is the wavelength used to calculated the FSR according to equation 2.11.

2.3 Hakki-Paoli Method

The peak gain as a function current density can be calculated from the P-I curves of lasers with different lengths as done in chapter 6, but in order to measure the gain spectrum a more elaborate method is required. An often used method is the Hakki-Paoli method, first described by Basil W. Hakki and Thomas L. Paoli in first half of the 1970's while working at Bell Laboratories [1]. In general it calculates the net gain $\Gamma g(\lambda) - \alpha_i$ from the Amplified Spontaneous Emission (ASE) spectrum. By measuring the ASE-spectrum and relating the intensity maxima and minima of the spectrum, the net gain can be calculated.

From equation 2.9, the intensity transmitted from the first facet is

$$I_{out}(\lambda) = \overleftarrow{I}_{tot}(\lambda)(1 - R_1) = \frac{\overleftarrow{I}_0(1 + r_1r_2G)(1 - R_1)}{(1 - r_1r_2G)^2 + 4r_1r_2G\sin^2(\pi\lambda/\Delta\lambda_{FSR})} \tag{2.16}$$

where R_1 is the (power) reflectance of the first facet. Except for the linear gain $G = G(\lambda)$, the only unknown quantity in this equation is the constant $\overleftarrow{I}_0$. This lack of information can be solved by forming the ratio ρ between a maximum of equation 2.16, where the sine function equals zero, and a minimum, where it equals one,

$$\rho = \frac{I_{max}}{I_{min}} = \frac{(1 - r_1r_2G)^2 + 4r_1r_2G}{(1 - r_1r_2G)^2} \tag{2.17}$$

This expression leads to a quadratic equation in G. Keeping in mind that equation 2.9 is only valid below the lasing threshold, that is $|r_1r_2G| < 1$, and that the ratio ρ by definition is larger than one, the equation can be solved without ambiguity to

$$G = \frac{1}{r_1 r_2} \frac{\left(\sqrt{\rho} - 1\right)}{\left(\sqrt{\rho} + 1\right)} \tag{2.18}$$

With $G = e^{(\Gamma g - \alpha_i)L}$ this can be rewritten to the formula usually shown in connection with Hakki-Paoli measurements

$$\boxed{\Gamma g - \alpha_i = \frac{1}{L} \ln\left(\frac{\sqrt{\rho} - 1}{\sqrt{\rho} + 1}\right) + \frac{1}{L} \ln\left(\frac{1}{r_1 r_2}\right)} \tag{2.19}$$

In conclusion, by measuring the ASE-spectrum and forming the ratio between adjacent max and min intensities, the net gain spectrum can be calculated. The Hakki-Paoli method is for obvious reasons also called the max/min method. It is important to once more note that the max/min method only is valid below threshold, since equation 2.9 only is valid below threshold. This is however not a serious limitation, since the gain will clamp at threshold anyway.

As one maximum and one minimum is needed to calculate the gain, one point of the gain curve will be obtained per every maximum-minimum, in other words two points per FSR. However, as the gain changes slightly, even over such as small wavelength range as one half FSR, the ratio ρ is formed by the average of two neighboring maxima divided by the minimum between them. This gives one point of the gain curve for each minimum, or one point per FSR. This has the severe implication that the Hakki-Paoli method cannot be directly applied to a VCSEL due to its very long FSR. In order to get a good wavelength resolution of the gain spectrum, a laser with a short FSR (longer cavity) has to be used. On the other hand, a too short FSR will lead to problems resolving the ASE-spectrum, as will be discussed in chapter 7. The characterization of the active regions was performed on edge emitting Metal-Clad Ridge-Waveguide (MCRW) lasers, which will be described in more detail in chapter 5.

Chapter 3

Tunable MEMS-VCSEL

With the help of the equations introduced in chapter 2, the basic concept of a MEMS-VCSEL will now be discussed. The general idea of continuously tunable lasers is to change the free spectral range, see equation 2.11, in effect shifting the wavelength of the longitudinal modes of the cavity according to equation 2.14. The FSR is changed by changing the optical length of the cavity Ln_g. The refractive index can be changed by for instance electro-optic effects, while the length of the cavity can be changed by moving of one of the mirrors. In semiconductor lasers this is usually achieved by depositing the top mirror onto a movable MEMS-membrane, see figure 1.2(a), hence the name MEMS-VCSEL. The membrane should be either thermally or electro-statically actuatable.

The SUBTUNE tunable VCSEL cavity is formed by a backside dielectric Distributed Bragg Reflector (DBR) mirror on top of an electroplated Au heatsink and a topside thermally actuatable membrane with a dielectric DBR mirror, see figure 1.2(a). By driving a current through the membrane, it is heated up and expands, changing the cavity length, effectively tuning the laser wavelength.

3.1 Distributed Bragg Reflector

Due to the short cavity, VCSELs need mirrors with a reflectances exceeding 99% in order to get mirror losses low enough to enable lasing. To achieve such high reflectivities, a type of layered mirrors called Distributed Bragg Reflectors (DBR) is used. A DBR consists of a layered stack of materials with alternating high and low refractive index. By making the layers one quarter wavelength thick, high reflectance is achieved for a wavelength span surrounding that wavelength. A computed DBR reflectance spectrum is shown in figure 3.1. The reflectance spectrum was computed using the transfer matrix method [6]. The DBR consists of 5 low-high index pairs of quarter wavelength thickness with refractive indices 1.43 (CaF_2) and 2.27 (ZnS) and has a center wavelength of 1.55 μm.

The wavelength span over which the DBR has a high reflectance is referred to as the DBR stopband. The width of the stopband is related to the refractive index difference between the high and low index materials. The maximum reflectivity is related to both the number

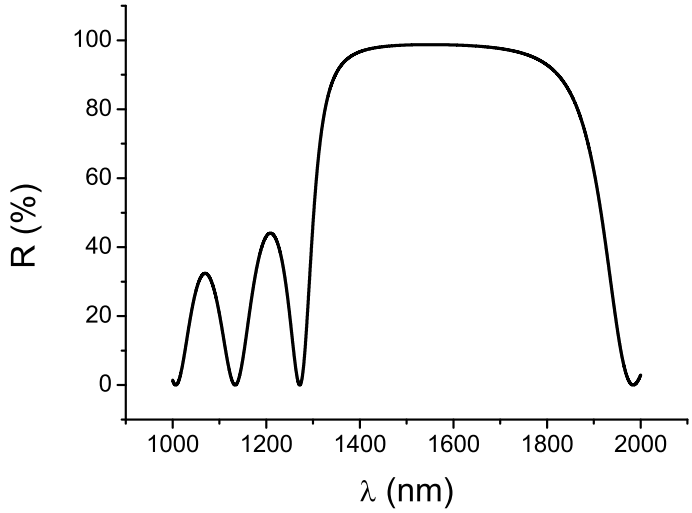

Figure 3.1: DBR reflectance spectrum with a maximal reflectance of 99.5%.

of layers, and the refractive index difference, with more layers and larger refractive index difference giving a higher maximum reflectivity. The DBR layers can be grown epitaxially, but then only materials with a small refractive index difference are available, making the DBR stopband relatively narrow and requiring many layers (usually 25-30 pairs) in order to achieve high enough reflectance. As an alternative, the DBR can also be realized by depositing dielectric materials which have a large refractive index difference of around 0.5-1. By using dielectric materials, high reflective DBRs with a large stopband can be achieved already at 5 pairs, see figure 3.1.

3.2 Wavelength Tuning

From equation 2.13 it is known that net the gain should equal the mirror losses during lasing. This can be graphically seen by plotting the mirror losses and net gain, $\Gamma g - \alpha_i$, in the same plot, see figure 3.2. This figure requires some explaining. The net gain is approximated by a parabolic function, with the maximum achievable net gain plotted with a blue dashed line. The mirror losses are plotted with a black line. It is calculated from the DBR previously discussed in section 3.1, assuming that the gold-electroplated bottom mirror has a reflectance of 100%. The positions of the longitudinal modes of the cavity are marked by vertical lines. Lasing can only occur at wavelengths where the net gain can equal the mirror losses. Thus, the wavelength interval over which lasing can occur is the region where the max net gain is larger than the mirror losses, in this example roughly from 1500 to 1600 nm. This interval will be referred to as the lasing interval. Only the mode positioned within this interval with the smallest mirror losses will lase, clamping the gain. The lasing mode wavelength is marked with a vertical red line and the clamped gain is plotted with a red curve.

As the length of the cavity changes, the positions of the longitudinal modes change. The

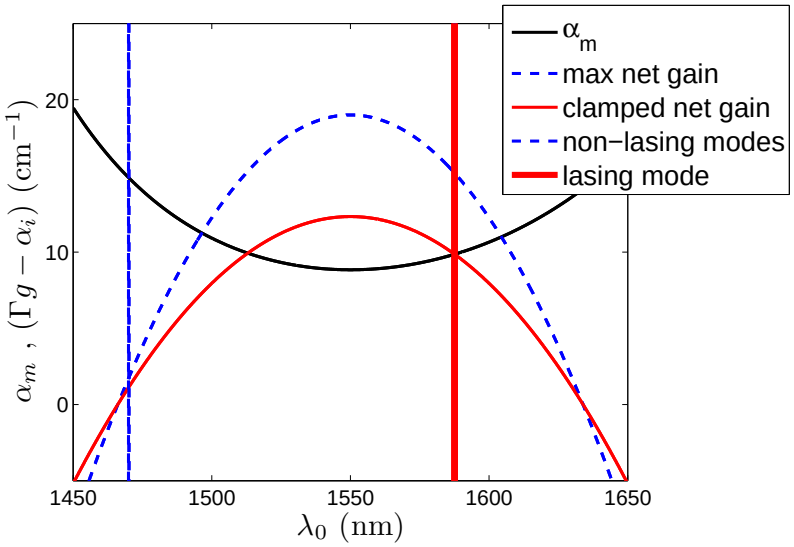

Figure 3.2: Schematic description of lasing in a MEMS-VCSEL.

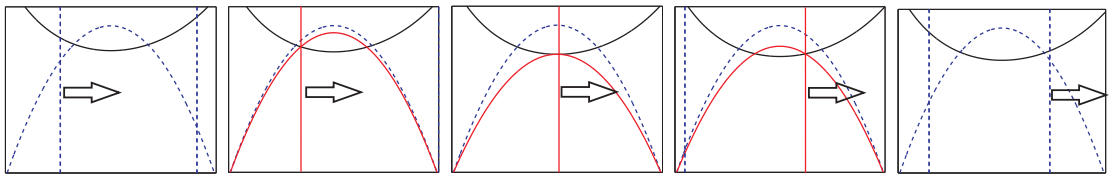

Figure 3.3: Schematics of a short cavity (long FSR) MEMS-VCSEL. The curves are explained in figure 3.2. As the cavity length continuously increase from (a) to (d) the modes move towards longer wavelengths. (a) No mode is lasing. (b) The mode starts to lase. (c) The mode has the smallest mirror losses, thus requiring the smallest net gain, and therefore has the lowest threshold current. (d) The mode is about to stop lasing. (e) Again no mode is lasing. If the cavity length keeps increasing, the next mode coming from the left will start lasing, see figure 3.4. Note that the mirror losses only change very slightly during tuning, since the change in cavity length is small.

tuning of the MEMS-VCSEL is schematically depicted in figure 3.3. The tuning range is clearly limited by the lasing interval, as seen also in figure 3.4(a). However, if the free spectral range is smaller than the lasing interval, the maximum tuning range will be the FSR. This is because two modes will be inside the lasing interval, while only the one mode with the lowest mirror losses will lase. This can be seen in figure 3.4(b).

The tuning range is thus limited by either the spectral width of the net gain and the mirror losses or the FSR. The tuning limit originating from the net gain-mirror losses can be increased by either increasing the width of the net gain, or decreasing the mirror losses (increasing mirror reflectivity and stopband). The tuning limit due to the FSR can be avoided by increasing the free spectral range, in other words decrease the length of the cavity.

The model used to describe the tuning of a MEMS-VCSEL is only meant to show the basic principles and has several very severe simplifications. As the wavelength is tuned, the posi-

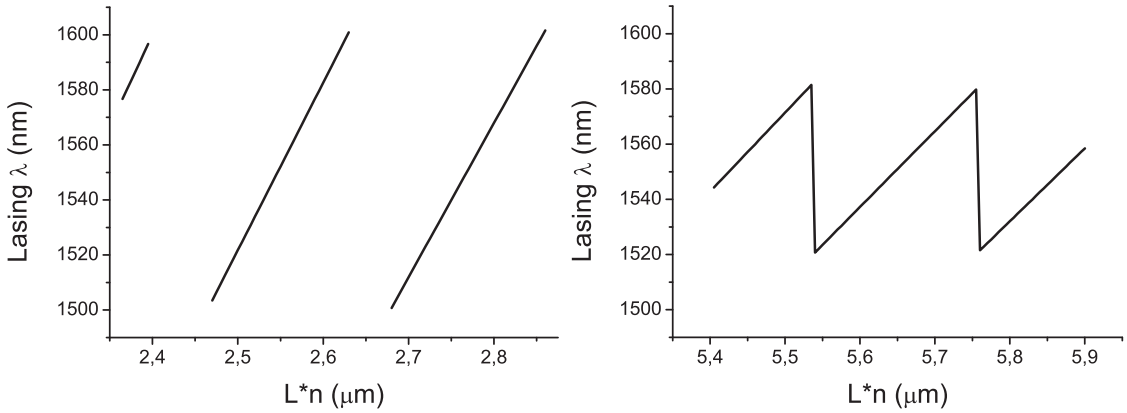

Figure 3.4: The lasing wavelength as a function of cavity optical length. (a) Simulated tuning of a MEMS-VCSEL with an FSR larger than the lasing interval. The tuning range is here equal to the lasing interval. Note that there are cavity lengths at which the laser does not lase since no mode has enough net gain to overcome the mirror losses. (b) Simulated tuning of a MEMS-VCSEL with an FSR shorter than the lasing interval. Here the tuning range is equal to the FSR.

tion of the resonant maxima and minima of the standing wave inside the cavity will change. This has several important implications. Firstly, the gain will change as the optical field at the quantum wells changes in magnitude. For maximum gain, a standing wave maximum is desired at the quantum wells. As the laser is tuned, this can be thought of as a wavelength dependent confinement factor. Secondly, it is important to note that the MEMS-VCSEL cavity actually consists of two coupled cavities, one in the semiconductor and one in the air-gap below the membrane, see figure 1.2(a). The reflections at the semiconductor-air interface serves to increase the feedback into the semiconductor part, increasing the gain. As the standing wave moves, changing the field strength at the interface, the reflection changes, altering the gain. Both these important effects have been completely neglected in the above model. The previous discussion and graphs should therefore be considered an attempt to motivate the need for a high and broad gain to improve the MEMS-VCSEL tuning range. The numbers presented should not be taken too seriously.

Chapter 4

Optical Gain in Semiconductors

In the previous chapter, it was seen that the width of the gain spectrum is one of the properties limiting the tuning range of a MEMS-VCSEL. This chapter will focus on the origin of the optical gain, and the most important factors influencing its magnitude and spectral range. This will later be used in explaining the results in chapter 8. Some basic properties of the semiconductor band structure will be described, followed by an investigation into the optical transition rates which will lead to an expression for the optical gain.

4.1 Band Structure

Interactions between photons and electrons across the bandgap of the semiconductor are the basis of any optoelectronic device. The bandgap is caused by Bragg reflection of the electrons against the periodic potential of the crystal lattice, resulting in an energy interval within which no states exist. The Bragg reflection is a function of the electron wavevector k, giving the conduction and valence bands a k -dependence, see figure 4.1. More specific, the bandgap E_g is defined as the energy difference between the lowest point in the conduction band E_C and the highest point in the valence band E_V, also called the conduction and valence band edges, see figure 4.1(a). A direct bandgap semiconductor, with the conduction and valence band edges located at the same k-value, is necessary for an efficient light emitter.

In most cases only the region in k-space with the band edges, plays an important role, see figure 4.1(b). In this region, the bands can be approximated by the commonly used isotropic parabolic band model [10],

$$E(k) = \frac{\hbar^2 k^2}{2m^*} \tag{4.1}$$

where m^* is the band effective charge carrier mass which differs from the rest mass, due to the influence of the crystal periodic potential. The valence band is degenerate with the so called Heavy Hole (HH) and Light Hole (LH) bands. This degeneracy can be lifted by

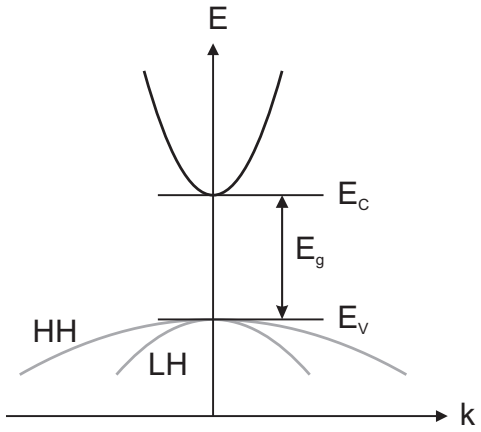

(a) Schematic picture of the band edges of a direct bandgap semiconductor using the isotropic parabolic band model.

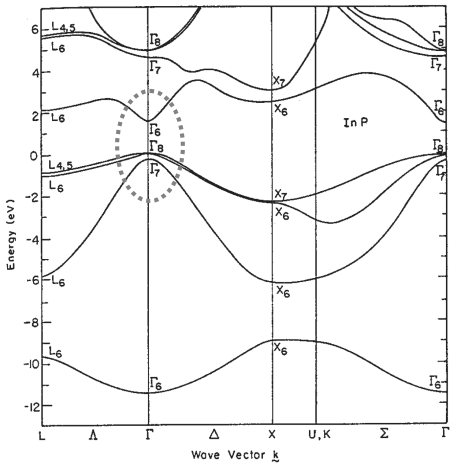

(b) Band structure of bulk InP with band edges marked. [8]

Figure 4.1: Energy bands of unstrained bulk InP.

introducing strain into the structure, see section 4.6. By using the isotropic parabolic band model from equation 4.1, the energy difference between the conduction and valence bands is

$$E_{21}(k) = E_g + \frac{\hbar^2 k^2}{2m_e^*} + \frac{\hbar^2 k^2}{2m_h^*} = E_g + \frac{\hbar^2 k^2}{2m_r^*} \tag{4.2}$$

where m_r^* is the reduced effective mass

$$\frac{1}{m_r^*} = \frac{1}{m_e^*} + \frac{1}{m_h^*} \tag{4.3}$$

A more detailed introduction to semiconductors can be found in for instance [9].

4.1.1 Bandgap Engineering

Different semiconductor materials have different bandgaps. By growing compound semiconductors with varying composition, the bandgap along a certain crystal direction can be tailored. This enables quantum wells to be grown in both the conduction and valence band. There will be some more details on this in chapter 5. In a quantum well, the one-dimensional quantum confinement will split the energy into subbands, see figure 4.2.

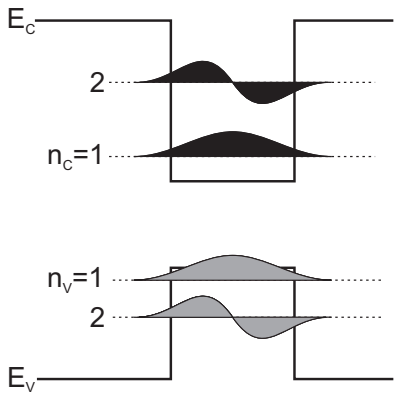

Figure 4.2: First two subbands envelope functions in a quantum well.

The Schrödinger equation needs to be solved in order to get the conduction and valence band energy states E_{C,n_C} and E_{V,n_V}, where the index subscript V can be either the light or heavy hole band. The indices n_C and n_V are the conduction and valence band quantum numbers. Due to the finite band offsets no analytical solutions for the energies exists. Note that this is the energy from the quantum well floor, making the energy difference between two states

$$E_{21} = E_g + E_{C,n_C} + E_{V,n_V} \tag{4.4}$$

4.2 Optical Transitions

In general three different optical interactions, or state transitions, between charge carriers in the conduction and valence bands are possible.

- An incoming photon with an energy larger than the bandgap, can stimulate an electron in the valence band to absorb the photon, exciting it up to the conduction band, see figure 4.3(a). This is referred to as absorption, or sometimes stimulated absorption, as the event is caused (stimulated) by the photon.
- An incoming photon stimulates an electron in the conduction band to fall down to the valence band, emitting a photon with energy corresponding to the bandgap. This emitted photon will have the same energy, phase and direction as the incoming photon, in all essence copying it. This transition is called stimulated emission, see figure 4.3(b).
- The transition of an electron from the conduction band to the valence band with the associated emission of a photon can also occur without being stimulated by a photon, see figure 4.3(c). Quantum-mechanically this is caused by so called vacuum-field fluctuations, while it semi-classically is referred to as spontaneous emission. The spontaneously emitted photon will have an energy corresponding to the bandgap, but in most relevant cases random phase and direction.

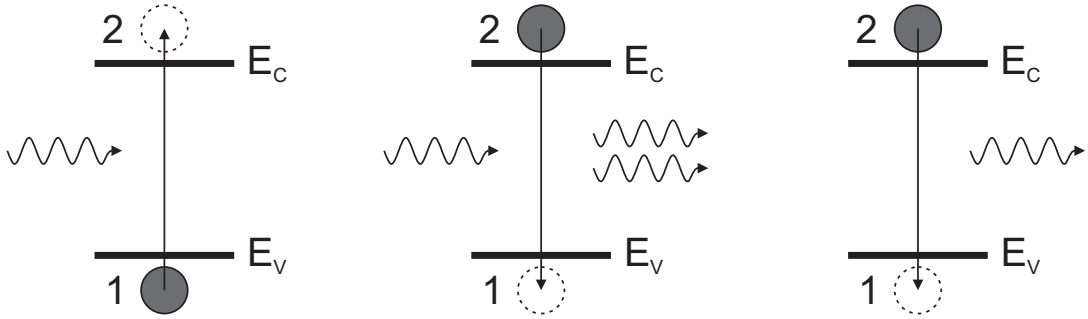

(a) Stimulated absorption (b) Stimulated emission (c) Spontaneous emission

Figure 4.3: The three different radiative band-to-band transitions.

In addition to the optical or radiative transitions, there are also a number of non-radiative recombination mechanisms, where an electron-hole pair recombine without the emission of a photon. Examples of such mechanisms are recombinations at defects or dislocations and Auger recombinations. The latter is a three-particle process, making it highly dependent on carrier density [6]. These will increase the threshold current of the laser.

4.3 Generation of Laser Light

The acronym LASER stands for Light Amplification by Stimulated Emission of Radiation and is, as the name implies, based on the process of stimulated emission. If the probability of stimulated emission can be made larger than absorption, one starting photon with phase and wavelength corresponding to a resonant mode will quickly be massively multiplied, giving the laser its coherent output.

In general a transition rate is proportional to the number of state pairs, that is in some sense the total density of electron-hole states between the two bands, times the probability that this pair is occupied by an electron-hole pair, times the probability that an individual transition will take place,

$$R_i = (\text{density of suitable state pairs}) * (\text{fraction of suitable state pairs occupied}) * (\text{transition probability}) \tag{4.5}$$

These factors will now be investigated, leading to a theoretical expression for the optical gain.

4.3.1 Density of States

The first factor of equation 4.5 is referred to as the density of states, $N(E)$. The density of states is defined as the number of states per unit energy and unit volume. For bulk material,

the density of states for the conduction band and valence band respectively is [6]

$$\begin{aligned} N_C(E) &= \frac{\sqrt{2}}{\pi^2}\left(\frac{m_e^*}{\hbar^2}\right)^{3/2}\sqrt{(E-E_C)} \\ N_V(E) &= \frac{\sqrt{2}}{\pi^2}\left(\frac{m_h^*}{\hbar^2}\right)^{3/2}\sqrt{(E-E_V)} \end{aligned} \tag{4.6}$$

where m_e^* is the effective electron mass, m_h^* is the effective hole mass accounting both the heavy and light hole bands. In a quantum well, the quantization significantly changes the density of states, which now has to be described for each subband according to

$$\begin{aligned} N_{C,n_C}(E) &= \frac{m_e^*}{\pi\hbar^2}H(E-E_C) \\ N_{V,n_V}(E) &= \frac{m_h^*}{\pi\hbar^2}H(E-E_V) \end{aligned} \tag{4.7}$$

where H is the Heaviside step function. The total density of states in each band is obtained by summing over all the subbands,

$$N_C(E) = \sum_{n_C}\frac{m_e^*}{\pi\hbar^2}H(E-E_C) \tag{4.8}$$

$$N_V(E) = \sum_{n_V}\frac{m_h^*}{\pi\hbar^2}H(E-E_V) \tag{4.9}$$

giving the QW density of states a step-like energy dependence. Since an optical transition requires both an occupied starting state and a free end state for the electron, the density of state pairs is used. The density of state pairs is referred to as the joint or reduced density of states.

$$\frac{1}{N_{red}\,(E_2-E_1)} = \frac{1}{N_C(E_2)} + \frac{1}{N_V(E_1)} \tag{4.10}$$

4.3.2 Occupation Probability

The second factor in equation 4.5 is the occupation probability. As electrons are fermions the occupation probability is governed by Fermi-Dirac statistics. The probability that a state of energy E is occupied at a temperature T is governed by the Fermi-Dirac distribution function

$$f(E) = \frac{1}{1 + e^{(E-E_F)/k_B T}} \tag{4.11}$$

where k_B is Boltzmann's constant and E_F is the so called Fermi level, defined such that $f(E_F) = 0.5$. With increasing temperature, more electrons will be found in states above the Fermi level. The probability of hole occupying a state is $1 - f(E)$.

The concept of the Fermi level can only be used for systems in thermal equilibrium. As semiconductor lasers are operated under high injection of charge carriers, the conduction and valence bands are far from equilibrium. However, the particles within each band are still in equilibrium, since the intra-band relaxation time is much smaller than the inter-band relaxation time [10]. This means that the Fermi-Dirac distribution can still be used, but with two different Fermi levels $E_{F,C}$ and $E_{F,V}$, for the conduction and valence band respectively. These are called quasi-Fermi levels. The position of the quasi-Fermi levels with respect to the band edges depends on the injection and the density of states.

4.3.3 Stimulated Emission and Absorption Rates

The stimulated absorption and emission rates, R_{12} and R_{21} respectively, can be analyzed using the joint density of states and the Fermi distribution. Using the states 1 and 2 according to figure 4.3 with $E_{21} = E_2 - E_1$ representing the photon energy of the transition, the rates can be stated as [6]

$$R_{12}(E_{21}) = R_r(E_{21}) f_1(E_1) \left[1 - f_2(E_2)\right] \tag{4.12}$$

$$R_{21}(E_{21}) = R_r(E_{21}) \left[1 - f_1(E_1)\right] f_2(E_2) \tag{4.13}$$

where R_r is a function of the joint density of states and the probability of a transition taking place. This factor is equal for upward and downward stimulated transitions. The gain in a semiconductor is directly proportional to the stimulated emission minus the stimulated absorption (all the energy dependencies will be dropped from now on to make the equations less messy)

$$R_{st} = R_{21} - R_{12} = R_r \left(f_2 - f_1\right) \tag{4.14}$$

which has to be larger than zero for the material to show gain. This can be investigated by requiring the ratio between f_2 and f_1 to be larger than one. By using equation 4.11 the ratio will be

$$\frac{f_2(E_2)}{f_1(E_1)} = e^{(\Delta E_F - E_{21}/k_B T)} > 1 \tag{4.15}$$

where $\Delta E_F = E_{F,C} - E_{F,V}$ is the separation between the conduction and valence band Fermi levels. Rewriting equation 4.15 gives the Bernard-Duraffourg condition for optical gain in semiconductors,

$$E_g < E_{21} < (E_{F,C} - E_{F,V}) = \Delta E_F \tag{4.16}$$

where the photon energy E_{21} of course has to be larger than the bandgap E_g.

To obtain the transition rate R_r, the Schrödinger equation has to be solved using the electrical field as a perturbation to the Hamiltonian. Further details on this can be found in [6]. Solving the time-dependent Schrödinger equation gives Fermi's golden rule,

$$R_r = \frac{2\pi}{\hbar} |H'_{21}|^2 N_{red}(E_{21}) \tag{4.17}$$

where H'_{21} is the matrix element representing the strength of the transition from state 2 to 1.

Matrix Element H'_{21}

The matrix element is especially important in QW lasers as it determines between which subbands transitions can take place. It can be written as

$$H'_{21} = \langle \psi_2 | H' | \psi_1 \rangle = \int \psi_2^* H'(\mathbf{r}) \psi_1 d^3\mathbf{r} \tag{4.18}$$

where ψ_2 and ψ_1 are the electron wavefunctions of the starting and final states. With the Bloch function formalism the wavefunctions can be written as a product of a Bloch function $u(\mathbf{k}, \mathbf{r})$ and the envelope function $F(\mathbf{r})$,

$$\psi(\mathbf{r}) = u(\mathbf{k}, \mathbf{r}) F(\mathbf{r}) \tag{4.19}$$

H' in equation 4.18 is the term perturbing the Hamiltonian,

$$H' = \frac{q}{2m_0} \mathbf{A} \cdot \mathbf{p} \tag{4.20}$$

where $\mathbf{A}$ is the vector potential of the electric field and $\mathbf{p}$ is the momentum operator. By assuming a time-harmonic electric field ($|\mathbf{E}|^2 = \omega^2 |\mathbf{A}|^2$), the integral in equation 4.18 can be written as

$$|H'_{21}|^2 = \frac{q^2 |\mathbf{E}|^2}{4 m_0^2 \omega^2} |M_T|^2 \tag{4.21}$$

where ω is the angular frequency of the optical field, $\mathbf{E}$ is the optical field strength and m_0 is the electron mass. M_T is a matrix element representing the strength of the transition. It

consists of a material constant and the overlap of the F_1 and F_2 envelope functions from equation 4.19

$$|M_T|^2 = \text{const} \cdot |\langle F_2|F_1\rangle|^2 \tag{4.22}$$

This causes selection rules for quantum wells due to the envelope function overlap. As seen in figure 4.2, only envelope functions with equal quantum number $n_V = n_C$ have a good overlap. This can be stated as

$$|\langle F_2|F_1\rangle|^2 \approx \delta_{n_C,n_V} \tag{4.23}$$

where δ is the Dirac delta function. The transitions between quantum well subbands with equal quantum number $n_V = n_C$ is referred to as allowed transitions, while transitions between subbands of different quantum numbers are called forbidden. Despite the name forbidden, these transitions do exist. The differences in effective mass and barrier height in the conduction and valence band cause the envelope functions to not be fully orthogonal to each other. The overlap of the allowed functions is in spite of this close to one, while the forbidden transitions have an overlap close to zero.

To achieve gain between the second order subbands, the quasi-Fermi levels need to be quite far from each other. Due to this, the $n_C = n_V = 1$ transition is in most cases the strongest, dominating a QW laser. In addition, the finite QW band offsets reduce the number of QW states to just a couple.

4.3.4 Expression for Optical Gain

Equations 4.14, 4.17 and 4.21 gives the total rate of stimulated processes

$$R_{st} = \frac{\pi}{\hbar}\frac{q^2\,|\mathbf{E}|^2}{2m_0^2\omega^2}\,|M_T|^2\,N_{red}(E_{21})(f_2 - f_1) \tag{4.24}$$

So far the net change R_{st} of the number photons per time due to stimulated emission and absorption has been expressed. In most applications it is more useful to work with an optical gain per unit length, defined as the increase of the photon density N_p per unit length. This can be related to the rate R_{st} via the group propagation velocity of the photons $v_g = c/n_g$,

$$g = \frac{1}{N_p}\frac{dN_p}{dz} = \frac{1}{N_p}\frac{dt}{dz}\frac{dN_p}{dt} = \frac{1}{N_p v_g}R_{st} \tag{4.25}$$

The energy density U of the electric field can be written both in terms of the photon density and the electric field strength [6],

$$U = N_p \hbar\omega \tag{4.26}$$

$$U = \frac{1}{2} n n_g \epsilon_0 |\mathbf{E}|^2 \tag{4.27}$$

giving the photon density as

$$N_p = \frac{n n_g \epsilon_0 |\mathbf{E}|^2}{2\hbar\omega} \tag{4.28}$$

where n and n_g are the mode and group refractive indices. Using this and the expression for the total stimulated emission rate in equation 4.25, the gain can finally be expressed as

$$\boxed{g(E_{21}) = \frac{1}{E_{21}} \frac{\pi q^2 \hbar}{m_0^2 n c \epsilon_0} |M_T|^2 N_{red}(E_{21}) (f(E_2) - f(E_1))} \tag{4.29}$$

For a quantum well, the gain is obtained by summing over all subband pairs

$$g(E_{21}) = \sum_{n_C} \sum_{n_V} g(n_C, n_V) \tag{4.30}$$

It is important to note that this model for the gain has its limitations. One problem is that Fermi's golden rule only considers one electron, neglecting the interactions between particles. A forward biased laser contains a high density of charge carriers, turning the calculation of the gain into a multi-body problem.

4.4 Gain Spectrum Features

Equation 4.29 will now be analyzed to determine the most important features of the gain spectrum. The two main interests are the dependencies on current and temperature. It is important to remember that the gain will clamp at threshold, and most of the features discussed in this section are valid until threshold. The described features will be used to explain the results in chapter 8.

4.4.1 Spectral Width

The gain spectrum width is determined by the Bernard-Douffbourg condition, previously stated as equation 4.16, which states that photons with energies between the bandgap and the quasi-Fermi level separation ΔE_F experience gain. The quasi-Fermi level separation, forming the upper gain limit, is dependent on the carrier density, with increasing carrier

density giving a larger separation. The carrier density in the quantum well will increase with the injected current until threshold, when it will clamp.

The lower limit of the gain, the bandgap energy, is also affected by the carrier density. At high densities, the charge carriers locally screen out the attractive forces of the crystal atoms. This makes the effective crystal potential weaker, resulting in weaker bound electrons. The electron wavefunctions will be less localized, giving rise to a broadening of the energy bands. In effect, this reduces the bandgap. This is referred to as bandgap shrinkage and can be described empirically according to

$$\Delta E_g = -bN^{1/3} \tag{4.31}$$

where b is a constant and N is the carrier density in three or two dimensions for bulk and QW material respectively. The bandgap in a forward biased QW laser shrinks on the order of 20-30 meV (35-55 nm in photon wavelength at 1.55 μm) compared to the thermal equilibrium bandgap [6]. The bandgap also decreases slightly with temperature.

4.4.2 Peak Gain

The position of the gain peak is dependent on both the quasi-Fermi level separation and the density of states. For a quantum well with the flat, step-like density of states, the peak gain wavelength only depends only on the quasi-Fermi level separation. Since the highest inversion is achieved at the band edge according to the Fermi-Dirac distribution function from equation 4.11, the peak gain would also be expected at the band edge. The peak does, however occur at slightly higher energies due to lineshape broadening [6]. In bulk material the peak gain is blue-shifted as ΔE_F increases with increasing current until threshold, due to the continuous increase in N_{red} for higher energies, see equation 4.6. A slow blue-shift with increasing current injection is also seen in a QW, even though the density of states in equation 4.7 consists of discreet steps.

The magnitude of the peak gain is determined by many factors, the most important again being the density of states and the Fermi level separation. As the temperature increases, the Fermi-Dirac distribution, equation 4.11 will broaden, reducing the carrier density for a specific energy. This will reduce and flatten the gain with increasing temperature.

4.5 Empirical Gain Relation

The dependence of the injection of current on the max optical gain of a quantum well is often empirically approximated as having a logarithmic dependence on the current density [6]

$$g\left(J\right) = g_0 \ln\left(\frac{\eta_i J}{J_{tr}}\right) \tag{4.32}$$

where g_0 is an empirical material gain constant, J is the injected current density and η_i is the internal quantum efficiency. J_{tr} is the transparency current density at which the material would be transparent, that is $g(J_{tr}/\eta_i) = 0$. Note that this equation only is valid until threshold, as the gain thereafter will be clamped and will no longer increase with current density. This equation will be frequently used when analyzing the measured gain curves in chapter 7 and 8.

The efficiency of a laser is highly dependent on achieving a high gain with a low current density. This is measured by the differential gain

$$\frac{dg}{dJ} = \frac{g_0}{\eta_i J} \tag{4.33}$$

4.6 Compressively Strained QWs

The use of compressively strained QWs has a significant influence on the optical gain. The compressive strain will lift the degeneracy of the heavy and light hole bands seen in figure 4.1(a) and only the heavy hole band will be important. In addition the matrix element M_T for Transverse Magnetic (TM) transitions is reduced, and Transverse Electric (TE) transitions will dominate [6], see also figure 5.3.

The strain also affects the effective masses, particularly in the valence band. The significant decrease in effective valence band mass decreases the valence band density of states, see equation 4.7. Thus, for a given hole density, the valence band quasi-Fermi level will penetrate further into the valence band. This increase in the quasi-Fermi level separation due to the compressive strain will reduce J_{tr} with up to 50% [6]. The differential gain will also be increased. The slope of the Fermi-Dirac distribution is the highest at the Fermi level, meaning that a slight movement of the Fermi-level will make a significant change in the carrier density at that energy. By moving both the valence and conduction band quasi-Fermi levels closer to the band edges, a smaller change in the position of the quasi-Fermi levels is needed to change the carrier densities close to the band edge. This increases the differential gain up to a factor of two [6].

Chapter 5

MCRW Lasers

As described in the section 2.3, the gain spectrum cannot be measured directly on a VCSEL due to its too long free spectral range. A laser with a shorter FSR is needed, making edge emitting lasers suitable. The Metal-Clad Ridge-Waveguide (MCRW) laser was chosen to characterize the active regions due to the current confinement provided by the ridge, making pumping of a narrow width of the active region possible, and easy fabrication. The MCRW laser was developed in the 1970's for applications in optical communication but is nowdays mostly used for material characterization. This chapter will first briefly describe the epitaxial growth and layer structure of the sample. Then the design of the MCRW lasers will be discussed, followed by an overview of the processing of the samples into MCRW lasers.

5.1 Epitaxial Growth

The active regions of Quantum Well (QW) laser diodes require epitaxial growth of compound semiconductor heterostructures with sharp interfaces of nanometer precision. There are two main ways of achieving this:

- **Molecular Beam Epitaxy:** MBE is a physical vapor deposition technique. High-purity materials are heated within so called effusion cells, evaporating atoms and molecules within an ultra high vacuum (UHV) deposition chamber. Due to the long mean free path length, the atoms and molecules travel basically collisionless to the substrate where they stick to the surface. On the heated substrate the atoms diffuse around, finally binding at an energetically favorable position, accomplishing epitaxial growth. By controlling shutters of the effusion cells, sharp interfaces between different compound semiconductor materials can be achieved. The UHV makes this fabrication method expensive, relatively slow and hard to calibrate. On the other hand it is possible to use low growth temperatures, very low background doping can be achieved and a wide range of different materials can be grown.
- **Metal-Organic Vapor-Phase Epitaxy:** In MOVPE, gaseous molecules containing the necessary atoms reacts at the sample surface. At temperatures of several hundred degrees centigrade, the molecules thermally decompose, with the intended atoms being

adsorbed to the substrate surface. The high growth temperatures give a high surface mobility, resulting in homogenous growth and a good material quality. By precisely controlling the gas flow, sharp interfaces between different compound semiconductor materials can be achieved. The group-III elements are supplied by metal-organic compounds called precursors such as trimethylgallium $Ga(CH_3)_3$, trimethylindium $In(CH_3)_3$ and trimethylaluminium $Al(CH_3)_3$, while the group-V elements are supplied from hydrides such as arsine AsH_3 and phosphine PH_3. MOVPE has become the most commonly used industrial technique for the growth of compound semiconductors for solar cells, lasers and light emitting diodes, due to the high growth rate and no need for expensive UHV equipment.

Laser samples used in this thesis were grown by Molecular Beam Epitaxy.

5.1.1 Active Regions

The epitaxial layer structure of the MBE-grown AlGaInAs active region can be found in appendix B. By growing compound semiconductors with various compositions, the bandgap can be changed, enabling growth of heterostructures such as quantum wells and Separate Confinement Layers (SCH). The possible bandgaps/lattice constants with the GaInAsP and AlGaInAs material systems can be seen in figure 5.1. One important limitation is that only lattice matched or thin layers of strained materials may be grown without the creation of dislocations and other defects. By growing compressively strained quantum wells, active regions with wavelengths of up to 2.3 µm can be grown on InP substrates.

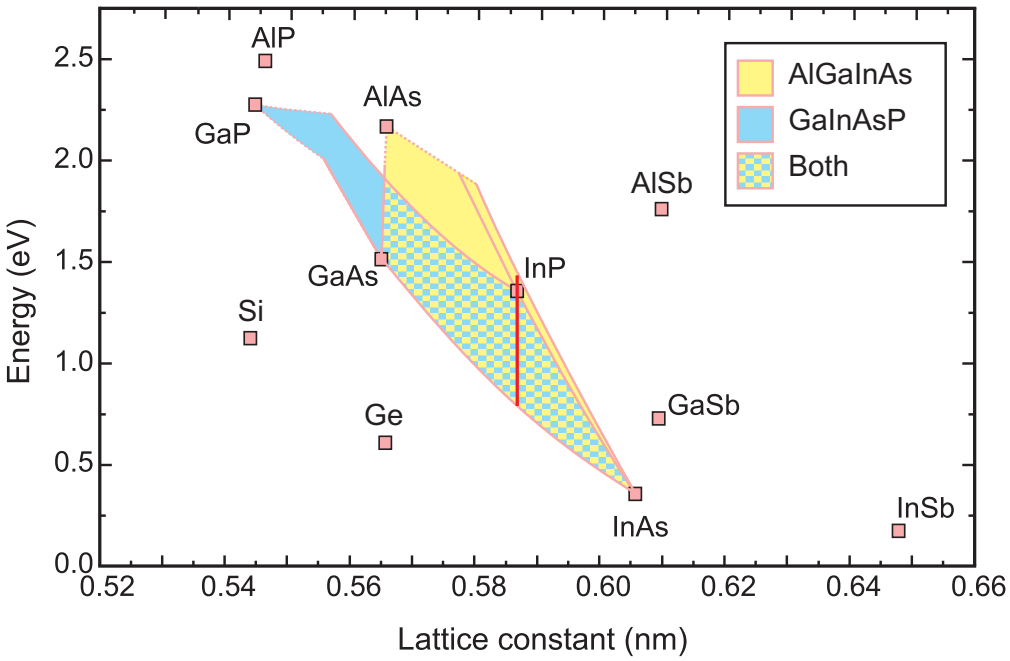

Figure 5.1: The semiconductors used in long-wavelength optoelectronics, with the material systems AlGaInAs and GaInAsP marked. The red line shows the bandgap range (ca 0.7-1.4 eV, 900-1700 nm) which can be grown lattice matched on InP substrates.

The MBE-grown AlGaInAs active region can be seen in figure 5.2. It has two compressively strained quantum wells surrounded by a relatively wide Separate Confinement Heterostructure, and an electron blocker in the conduction band to reduce electron leakage from the QWs. The compressive strain will lift the valence band degeneracy, making only the heavy hole band important for radiative transitions. From the band offsets, the conduction band quantum well was calculated to have only one subband, while the heavy hole valence band quantum well has two.

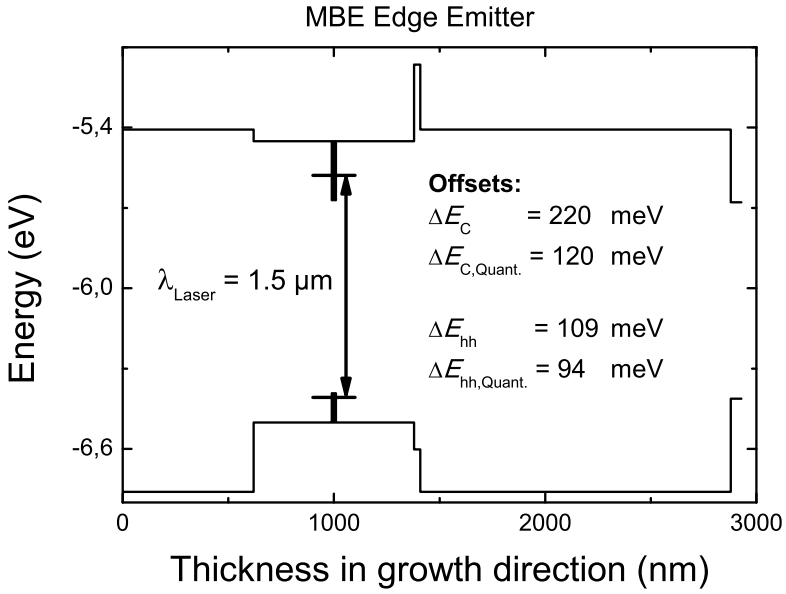

Figure 5.2: The MBE-grown active region. Electrons are injected through the substrate from the left, while holes are injected from the right.

5.2 Metal-Clad Ridge-Waveguide

In addition to gain, a semiconductor laser also needs waveguiding. The lower bandgap material in the QWs and SCH have a higher refractive index than the surrounding claddings, forming the vertical waveguiding of the MCRW laser, see figure 1.2(b). The mode intensity distribution along the vertical direction can be calculated by solving the wave equation, originating from Maxwell's equations, with appropriate boundary conditions [10]. The result of such a calculation gives the confinement factor for each layer. By estimating the optical losses from free-carrier absorption and inter-valence band absorption in each layer, the optical losses of each material can be estimated [11]. By summing over all the m layers with layer optical losses $\alpha_{i,m}$ weighted with the corresponding confinement factors Γ_m, the total mode material losses α_i can be estimated as

$$\alpha_i = \sum_m \Gamma_m \alpha_{i,m} \tag{5.1}$$

In this way internal losses of α_i= 1.8 cm^{-1} were calculated for the vertical waveguide. The total vertical confinement factor for the two QWs was found to be 1.85%.

The lateral waveguiding is achieved by etching a ridge, forming an InP ridge waveguide, see figure 1.2(b). This forms three different regions in the lateral direction; the ridge, and one region on each side of it. In every of these three regions, a mode effective refractive index in the vertical direction can be calculated by summing the refractive index of each material weighted with the corresponding confinement factors, similar to the loss calculation in equation 5.1. By using these three effective indices, a three-layered waveguide is obtained in the lateral direction. The wave equation can now be solved in the lateral direction, yielding the lateral confinement factor. This method is called the effective refractive index method [6]. Such calculations showed that the fundamental optical mode is well confined under the ridge in the lateral direction.

Previous investigations [12] of the MCRW lateral waveguiding show that the MCRW supports both TE and TM modes, see figure 5.3. Whether the TE or TM modes has the highest lateral confinement factor depends on the effective refractive index step between the ridge and the regions outside the ridge. For small and large effective index steps, the TE mode has the highest lateral confinement, while intermediate effective index steps makes the TM mode lateral confinement factor larger than the TE. Since the samples were grown with compressively strained QWs, the TM gain could be assumed to be much smaller than the TE gain, see section 4.6. This means that even if the TM mode would be slightly better guided than the TE mode, the MCRW lasers will still be dominated by the TE mode.

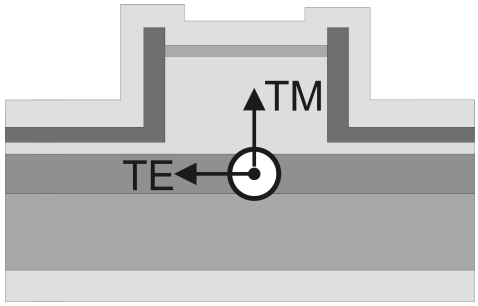

Figure 5.3: TE and TM modes in an MCRW laser.

From a calculation by a mode-matching technique, the reflectivities of the waveguide-air interfaces were taken to be 34% for the fundamental TE mode[13].

5.3 Lateral Carrier Diffusion

The MCRW laser enables pumping of a small active region width by injection of carrier through the ridge. However, underneath the ridge, the MCRW laser has no potential barriers to laterally confine the charge carriers. The injected hole current density profile will therefore slightly broaden below the ridge due to lateral carrier diffusion, see figure 5.4(a). Note that this is not a lateral current, as there is no electric field in the lateral direction moving the holes, but a diffusion proportional to the gradient of the hole density. As the maximum gain

is a function of the current density (equation 4.32), it is necessary to know the current density in the active region underneath the ridge where the optical mode is confined. This means that the lateral carrier diffusion has to be quantified. It is important to note that the hole density will clamp at threshold, meaning that the lateral carrier diffusion also should clamp. The lateral carrier diffusion will thereby act as an approximately constant leakage current above threshold.

This diffusion can be investigated by measuring the threshold current I_{th} for different ridge widths. As the ridge width w goes towards zero, the threshold current should ideally also go to zero according to

$$I_{th} = J_{th} w L \tag{5.2}$$

where J_{th} is the threshold current density and L is the laser length. Hence by extrapolating the threshold current against the ridge width, a straight line should go to the origin. This is, however, not the case due to the lateral carrier diffusion, see figure 5.4(b). The I_{th}-w curve has to be shifted to pass through the origin by adding an effective diffusion width w_{diff} that accounts for the lateral carrier diffusion. The lateral diffusion width w_{diff} is found as the intersection between the I_{th}-w_{ridge} curve and the x-axis, see figure 5.4(b). Due to the lateral carrier diffusion, the current density of the active region is given by an effective width $w_{eff} = w + w_{diff}$.

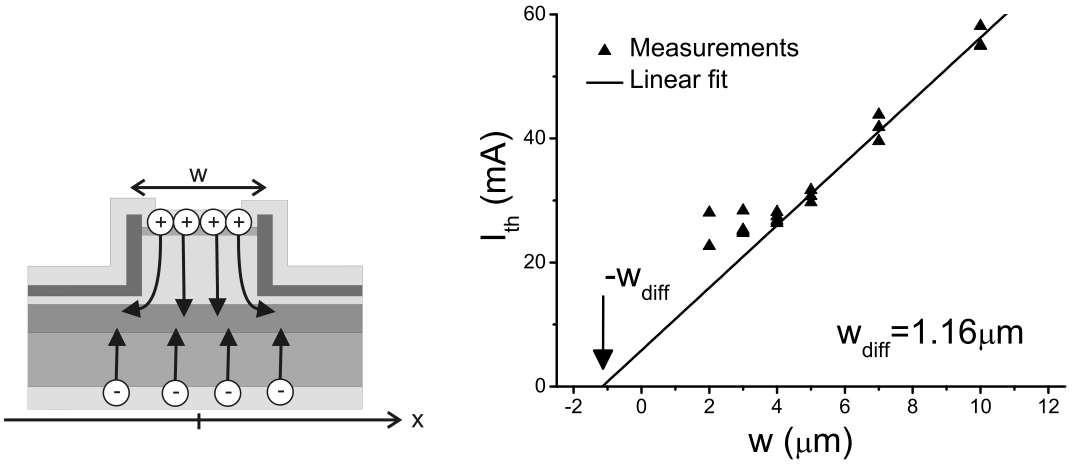

Figure 5.4: Lateral carrier diffusion. (a) Schematic figure of lateral carrier diffusion in a MCRW laser. (b) Measurement of w_{diff} by fitting 5,7 and 10 μm wide, 500 μm long lasers.

The lateral carrier diffusion can be avoided by etching through the active region. This would however create exposed etch surfaces inside the active region, which would act as recombination centers for bimolecular surface recombinations. A decision was made to not etch through the active regions, as the lateral diffusion current is a better documented phenomena and it was believed to be easier to deal with than surface recombinations. There might also be

other disadvantages of etching through the active region such as higher waveguide scattering losses.

5.3.1 Analytic Expression

To gain more insight, the lateral carrier diffusion can be analyzed analytically by considering a simplified model [14]. A one-dimensional equation for the hole density profile $p(x)$ is obtained from the current continuity equation as

$$D_{eff}\frac{\partial^2 p(x)}{\partial x^2} + \frac{J_{in}}{dq} - \frac{p(x)}{\tau} = 0 \tag{5.3}$$

where x is the lateral position with $x = 0$ corresponding to the middle of the ridge, see figure 5.4(a). The active region thickness is denoted by d, q is the elementary charge, D_{eff} is the effective diffusion coefficient, J_{in} is the current density injected into the ridge ($J_{in} = I/(wL)$) and τ is the carrier lifetime. By assuming a constant carrier lifetime τ, having the same value underneath and beside the ridge, this equation has the solutions [14]

$$p(x) = \frac{J_{in}\tau}{qd} e^{-|x|/L_D} \sinh\left(\frac{w}{2L_D}\right), \qquad |x| > \frac{w}{2} \tag{5.4}$$

$$p(x) = \frac{J_{in}\tau}{qd}\left[1 - e^{-w/2L_D}\cosh\left(\frac{x}{L_D}\right)\right], \qquad |x| < \frac{w}{2} \tag{5.5}$$

where $L_D = \sqrt{D_{eff}\tau}$ is the diffusion length. The average current density underneath the ridge can be calculated from the integral,

$$J_{under} = \frac{qd}{w}\int_{-w/2}^{w/2}\frac{p(x)}{\tau}dx = J_{in}\left[1 - \frac{L_D}{w}\left(1 - e^{-w/L_D}\right)\right] \tag{5.6}$$

from which it can be seen that as the ridge width decreases, the current density J_{under} obtained for a certain input current density J_{in} decreases, see also figure 5.5. This means that a larger portion of the injected carriers diffuse outside of the volume underneath the ridge in a narrower ridge. Thus, a narrow ridge laser must be pumped harder to achieve the same current density underneath the ridge and therefore the same gain. This is also seen in figure 5.4(b) where the threshold current against ridge width becomes non-linear for small widths. There may however be additional contributions to the unexpected high threshold currents for narrow ridges. As the width decreases, a larger portion of the optical field propagates close to the etched surfaces. These surfaces may be rough, increasing scattering losses. The smaller width will also reduce the lateral confinement factor. As the width goes towards zero, the lateral confinement factor will go to zero, implying that the threshold current would go towards infinity, but this is probably only important for very narrow ridges.

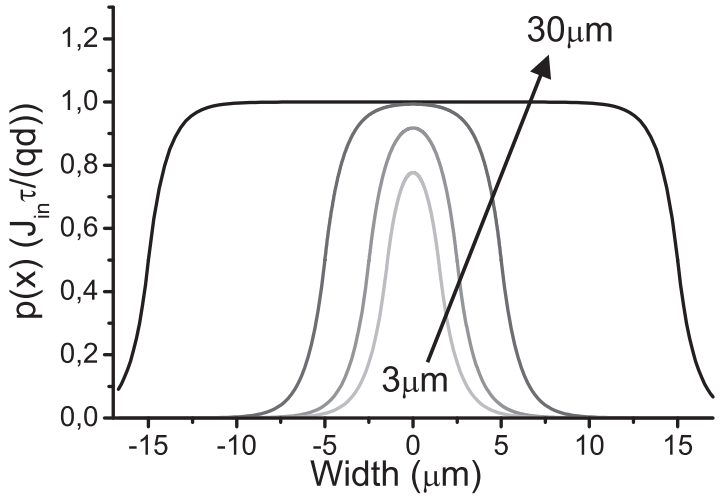

Figure 5.5: Equation 5.4 and 5.5 plotted for ridge widths of 3, 5, 10 and 30 μm with a diffusion length of 1 μm.

The concept of effective width, previously determined experimentally, can now be investigated using equation 5.6 and $J_{in} = I/(wL)$.

$$J_{under} = \frac{I\left[1 - \frac{L_D}{w}\left(1 - e^{-w/L_D}\right)\right]}{wL} = \frac{I}{w_{eff}L} \tag{5.7}$$

which gives the expression for the effective width

$$w_{eff} = \frac{w}{1 - \frac{L_D}{w}\left(1 - e^{-w/L_D}\right)} = w + w_{diff} \tag{5.8}$$

This gives an analytical expression for the lateral carrier diffusion width, previously experimentally determined from the PI-curves.

$$w_{diff} = \frac{L_D\left(1 - e^{-w/L_D}\right)}{1 - \frac{L_D}{w}\left(1 - e^{-w/L_D}\right)} \tag{5.9}$$

A plot of this equation can be seen in figure 5.6. The diffusion width has two limits; when $\frac{w}{L_D} \to 0$, the width goes towards $2L_D$, while when $\frac{w}{L_D} \to \infty$, it goes towards L_D.

This model has some important simplifications that should be pointed out. The carrier lifetime τ is not independent on the lateral position, since the lateral optical mode profile and therefore the photon density varies with x. A more correct, but complicated, approach would be to investigate the overlap between the optical mode and the gain profile originating from the carrier density profile which would then be dependent of each other via the carrier lifetime. Due to the smaller photon density beside the ridge, the carrier lifetime τ_{out} will be longer than τ. This will give a larger diffusion length outside the ridge, making the hole-density tails in figure 5.5 longer. Longer lifetimes mean that the carriers have more time to

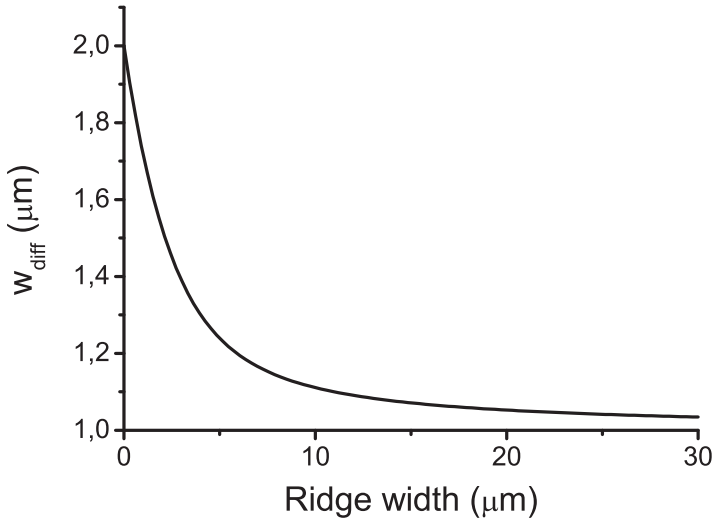

Figure 5.6: Equation 5.9 plotted with a diffusion length of 1 μm.

recombine non-radiatively and that many of the photons that diffuse out from the volume underneath the ridge will not contribute to the lasing.

It can be pointed out that from another point of view, the effective width can also be seen as a leakage current, decreasing the current density underneath the ridge from J_{in} to J_{under}. This is equivalent to shifting the I_{th}-w curve in vertical direction in figure 5.4(b), and the leakage current at threshold current would be $I_L = I_{th} w_{diff}/w_{eff}$. As mentioned before, the carrier densities are clamped above threshold, meaning that the lateral carrier diffusion will not increase above threshold, unless τ_{out} changes with the increasing photon density underneath the ridge. Since the optical mode is well confined underneath the ridge, no significant change in τ_{out} should be expected. This agrees reasonably well with an investigation in [14] which found that the differential efficiency (see section 6.2) was only slightly affected by the lateral carrier diffusion. The current above threshold can therefore be written as

$$I = J_{under} wL + I_L \qquad \rightarrow \qquad J_{under} = \frac{I - I_L}{wL} \tag{5.10}$$

This is however not very important to this work, as all gain spectra measurements are performed below threshold.

In conclusion, the simple analytical expression provides at least a part of the explanation for the unexpected high threshold currents for small ridges. By using a diffusion length of 1 μm, values of w_{diff} comparable to the experimental values were obtained, see figure 5.4(b). The diffusion width does not vary significantly for ridges wider than 5 μm, see figure 5.6. The gain characterization in chapter 8 was therefore done on 5 μm wide ridge MCRW lasers.

5.4 MCRW Process

This section will shortly describe the important process steps. The full MCRW process sheet can be found in appendix C, and the epitaxial layer structure in appendix B. A schematic figure of the whole process can be seen in figure 5.7.

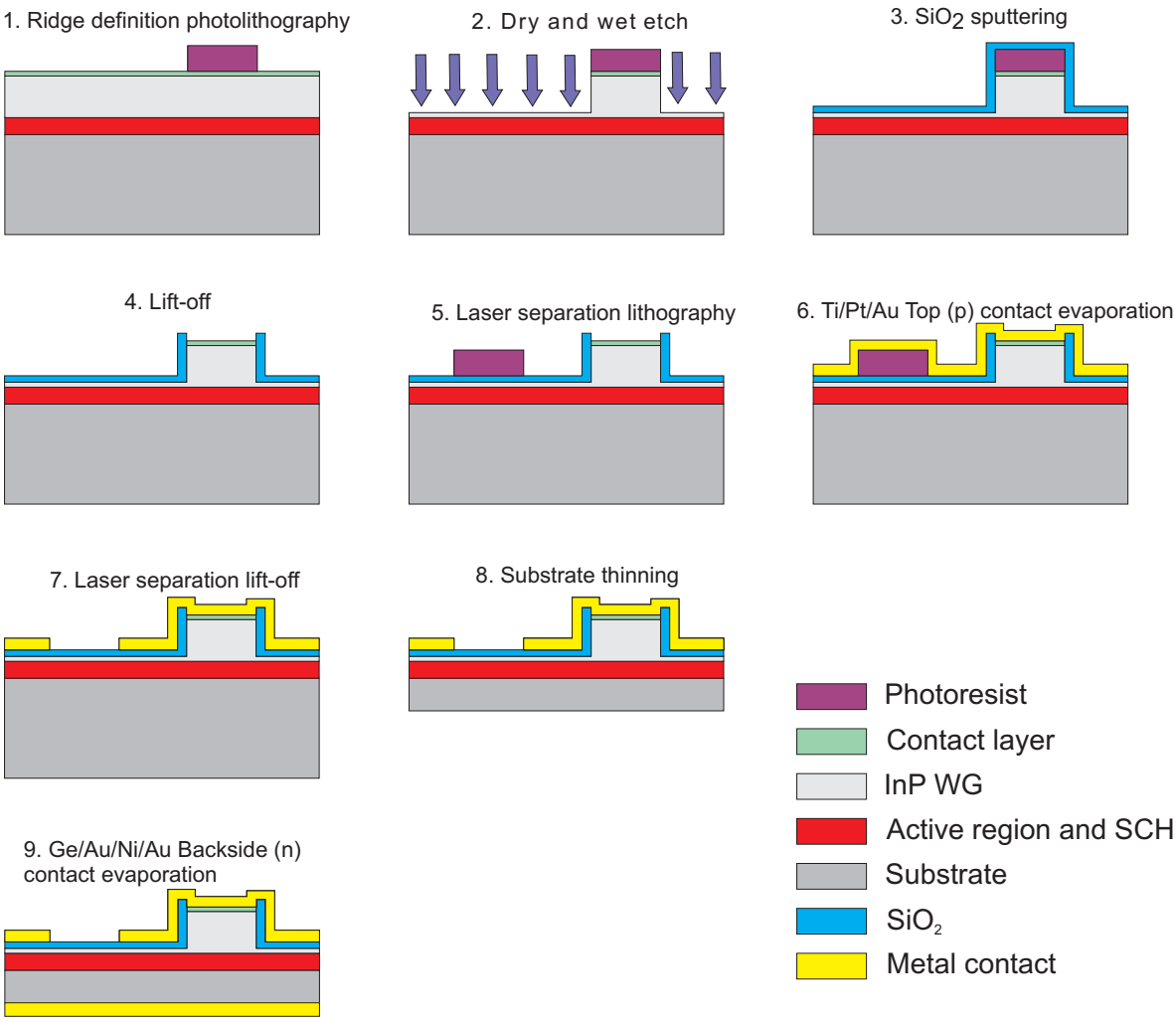

Figure 5.7: Schematic overview of the important process steps. Note that the layers are not in proper scale.

The ridges were defined by photolithography, see figure 5.7.1. The mask used had stripe widths w of 1, 2, 3, 4, 5, 7, 10 and 30 µm. The two smallest widths, 1 and 2 µm, did not stick during the development of the photoresist. Resist stripes from 3-30 µm could be developed in a good way.

5.4.1 Ridge Etching

Using the photoresist stripes as an etch mask, the InP layer was etched to form the ridge waveguide, see figure 5.7.2. In order to etch ridges with a width of just a couple microns more than 1.5 microns, a highly anisotropic etch was required. Dry etching was therefore used to etch the ridges, followed by a short wet etch to smoothen out any surface roughness from the dry etching.

Dry Etch

Dry etching of the GaInAs contact layer and InP waveguide was done with Electron Cyclotron-Resonance Reactive-Ion-Etch (ECR-RIE). Methane and nitrogen gasses are introduced into a low-pressure chamber, where a plasma is struck using a 2.45 GHz electromagnetic field and a static magnetic field. Due to the Lorentz force, electrons in a static magnetic field will move in a circle with the angular frequency of

$$\omega_c = \frac{qB}{m_0} \tag{5.11}$$

where B is the magnetic field, q the elementary charge and m_0 the electron mass. At a certain magnetic field B the angular frequency ω_c will equal the frequency of the electromagnetic field. The free electrons in the gas will then experience electron cyclotron-resonance. These circulating electrons will ionize the methane and nitrogen molecules by knocking away electrons in inelastic collisions. The ionized gas radicals are accelerated towards the sample by applying a DC potential difference between the sample and the plasma. The accelerated ions hit the sample surface, knocking out atoms from the sample. This gives rise to a physical anisotropic etch. The highly reactive radicals at the sample surface also cause a more isotropic chemical etch. The balance between the physical and chemical components of the etch can be adjusted by changing process parameters such as pressure and gas flow. The etched material is carried away in gas form.

Since the InP etch rate was quite modest at around 25 nm/min (for etch times around 10-15 min), etch times in excess of 50 minutes were required to etch away the $\sim$1.5 µm of the InP outside of the ridges. During such long etch times the photoresist will burn due to the heating of the sample. The burnt resist is more difficult to remove, making the following lift-off step more difficult, see figure 5.7.4. To avoid this problem, four to five etch steps of a maximum of 15 minutes were used, unloading the sample to let it cool in the vented load-lock between each etch step. This prevented the resist from burning. The InP etch rate was checked after each etch step by using InP dummies. Additionally, the quarter 2-inch wafer sample was found to etch 4-5% faster than the much smaller (ca 4x4 mm) dummies. This knowledge, etch rate measurements from dummies and the low etch rate made a precise control of the etch depth possible. The etch selectivity of InP against the photoresist (AZ5214) was found to be ca 2-2.5, meaning that the $\sim$1.7 µm thick resist was sufficient for the $\sim$1.5 µm InP etch.

The chlorine RIE etch was also tested. It showed several disadvantages compared to the ECR-RIE methane etch such as very fast etch rates, making it difficult to control the etch

depth, and a high sample temperature, almost instantly burning the resist. The ECR-RIE was therefore used for the dry etching of the ridges.

Wet Etch

The dry etch may result in slightly rough etch surfaces with reactants from the chemical etching remaining on the surface. The impinging ions also cause damage to the crystal structure in the vicinity of the surface. To remove these undesired defects, a short wet etch step was performed after the dry etch, removing the damaged layers and smoothening any surface roughness. The wet etch was done just before the SiO_2 passivation, see figure 5.7.3, and also served to remove any oxides. A number of different etchants were tried. The specifications required an etchant with a highly isotropic etch behavior to prevent an underetching of the ridges and a relatively slow etch rate to only etch away ca 20-40 nm of InP in a controlled manner. The etchant finally used was $HBr:Br_2:H_2O$ = 150:1:1800, which has previously shown good results in removing defects on the sidewalls after dry etching in the InP material system [15].

Etch Depth

The control of the etch depth was found to be crucial. Three different etch depths were tried.

- Leaving 1 µm of InP. The main purpose of this was to reduce the lateral index guiding, suppressing higher order transversal modes. However, no lasing was observed in the cleaved lasers.
- Etching all the way through the InP down to the AlInAs electron blocker, see appendix B. As the ECR-RIE does not etch Al-rich layers, a very precise control of the etch depth was not required. These lasers showed quite high threshold currents and an unsatisfactory yield.
- Leaving a ca. 50 nm thick layer of InP before the AlInAs grading layer. These lasers turned out to have low threshold currents with a good yield.

The last etch depth was used on the sample later characterized in chapters 6 and 8.

5.4.2 Process Finish

After the ridge etching, an SiO_2 passivation layer was deposited by sputtering, see figure 5.7.3. Contact windows were opened on top of the ridges by lift-off, figure 5.7.4. To separate the lasers, a second lithography was done before the top contact evaporation by electron beam evaporation and following lift-off, see figure 5.7.5-7. Before evaporating the backside contact, the substrate was thinned from approximately 350 µm to 150 µm to make cleaving of short lasers easier, see figure 5.7.8. The thinning was done by lapping the sample using Al_2O_3 grain. A microscope picture of the topside of the finished sample can be seen in figure 5.8.

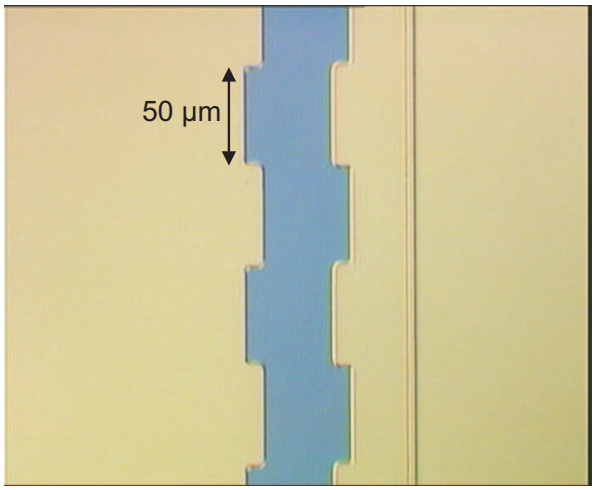

Figure 5.8: Microscope picture of a 5 µm wide ridge on the right side. The blue SiO_2 passivation and gold top contact is also be seen.

The processed samples were finally cleaved into lasers with lengths 300, 400, 500, 700, 900, 1100 and 1500 µm and mounted on a copper heatsink with conductive epoxy glue.

Chapter 6

P-I Characterization

The characterization of the MCRW lasers and the active region by output light power against input current (P-I curve) measurements will be described in this chapter. The measurements are based on the theory described in chapter 2, 4 and 5. All measurements were performed during Continuous Wave (CW) operation unless otherwise specified.

A P-I and U-I measurement can be seen in figure 6.1. The threshold current I_{th} is defined as the current at which lasing starts and the gain clamps. This is extracted from the P-I curve by a linear extrapolation of the above-threshold part of the curve to zero power. A threshold current of 26 mA was obtained for 500 µm long and 5 µm wide lasers. By measuring the P-I curves for lasers of different lengths and ridge widths, several important properties of the lasers can be obtained. These will be needed in the analyzing of the measured gain spectra in chapter 8.

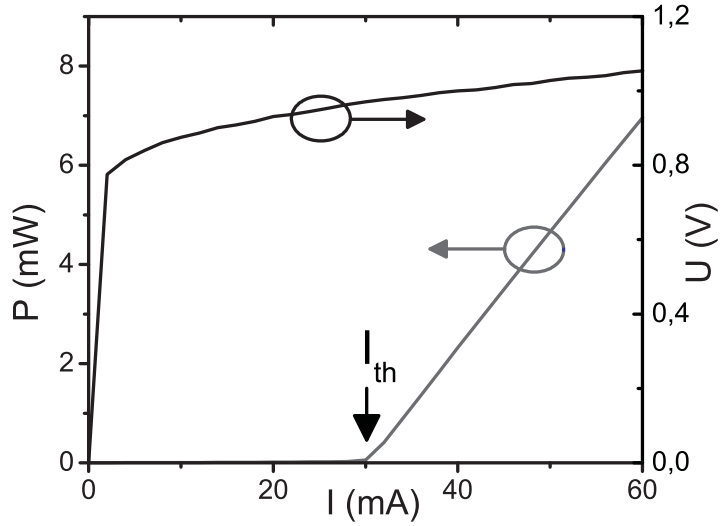

Figure 6.1: P-I and U-I curves of a laser with a threshold current of 30.1 mA.

6.1 Lateral Carrier Diffusion

The lateral carrier diffusion width is an important property as the gain is fitted, according to equation 4.32, using the current density. The lateral diffusion width was extrapolated from the PI-measurements as described in section 5.3. Due to the non-linear behavior of narrow ridge lasers, the effective lateral diffusion width w_{diff} was extrapolated using lasers with ridge widths of 5,7 and 10 µm. As seen in figure 5.6, no significant difference in the lateral diffusion width is expected for the 5, 7 and 10 µm wide ridges. The extrapolation for lasers of different lengths can be seen figure 6.2. It is interesting to note that the 300 µm long lasers have the highest threshold currents. This is a normal behavior explained by equation 6.1 and 6.5, according to which I_{th} depends on the length both linearly and exponentially. The results are presented in table 6.1.

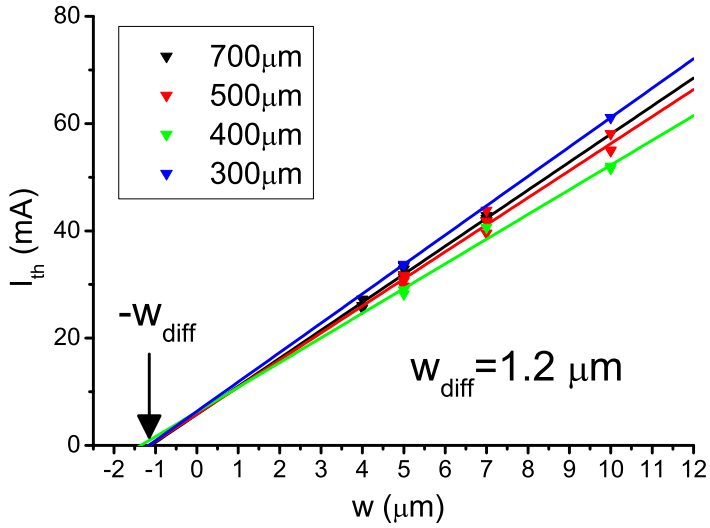

Figure 6.2: Extrapolation of w_{diff} at 15^{o}C.

Length (µm)	w_{diff}
700	1.11
500	1.16
400	1.35
300	1.16
average	1.20

Table 6.1: Table of w_{diff} extrapolated for widths 5,7 and 10 µm for MCRW lasers of different lengths measured at 15^{o}C.

These results agree well with the analytical model described in section 5.3 for a diffusion length of 1 µm. As seen from table 6.1, w_{diff} does not show any significant difference or trend for different lengths. According to [14], the diffusion length and therefore the diffusion width should decrease slightly for higher temperature and current density. However, since no increase was seen from the data, the dependence of the current density on w_{diff} was assumed to be small enough to be neglected. This means that a constant portion of the injected current

leak out of the active region until threshold, when it clamps. A diffusion width of 1.2 µm was therefore used for the used ridge widths 5,7 and 10 µm at all currents below threshold and all heatsink temperatures. Below threshold, the current density injected into the active region underneath the ridge can now be calculated as

$$J = \frac{I}{L(w + w_{diff})} \tag{6.1}$$

Observe that this means that the average lateral carrier diffusion is w_{diff}/2=0.57 µm on each side of the ridge.

6.2 Efficiency and Internal Losses

The efficiency of the laser can also be obtained from the P-I curve. The slope of the P-I curve above threshold, is the differential quantum efficiency

$$\eta_d = 2\frac{q\lambda}{hc}\left(\frac{dP}{dI}\right)_{\text{above threshold}} \tag{6.2}$$

where the factor 2 accounts for that only the output power from one facet is measured. The differential quantum efficiency is a measure of the fraction of the input carriers that contribute to the output laser power. In order to measure it properly, it is important to make sure that all the emitted light is measured. Otherwise η_d will be too low. To capture as much as the emitted light as possible, a detector with a diameter of 5 mm was used and positioned as close to the laser as possible. The differential efficiency is related to other laser parameters as [10]

$$\eta_d = \eta_i \frac{\alpha_m}{\alpha_i + \alpha_m} \tag{6.3}$$

where η_i is the internal quantum efficiency (sometimes also called the injection efficiency), representing the fraction of the injected charge carriers that produce carriers in the active region, and the second factor is the ratio of the useful photon losses (mirror outcoupling losses) to the total photon losses. This can be rewritten to

$$\frac{1}{\eta_d} = \frac{1}{\eta_i} + \frac{1}{\eta_i}\frac{\alpha_i L}{\ln(1/R)} \tag{6.4}$$

using the mirror losses from equation 2.13. By plotting this equation for lasers with different lengths, η_i and α_i can be obtained from a linear fit, see figure 6.3.

The internal losses of 1.7 cm^{-1} compares very well to the estimated material losses of 1.8 cm^{-1}, meaning that no extra losses are expected from the lateral waveguide. The wet etch step, designed to smoothen out any etch surface roughness, described in section 5.4.1 seems to have worked well.

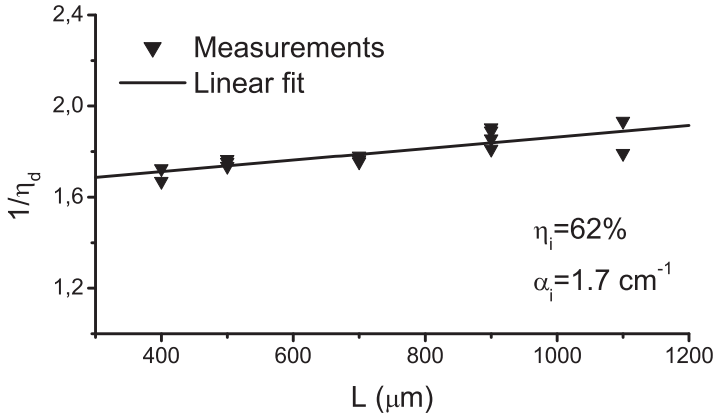

Figure 6.3: $1/\eta_d$ vs L for 5 μm wide lasers at 15^{o}C.

6.3 Threshold Current at Infinity Length

By combining the empirical QW gain equation in equation 4.32 with the lasing intensity condition from equation 2.13, an expression for the threshold current density is obtained

$$J_{th} = \frac{J_{tr}}{\eta_i} exp\left[\frac{\alpha_i}{\Gamma g_0} + \frac{1}{\Gamma g_0}\frac{1}{L}\ln\left(\frac{1}{R}\right)\right] \tag{6.5}$$

This equation can be used to plot the threshold current density against the inverse length, see figure 6.4. By extrapolating the threshold current density to infinity length, an important figure of merit for quantum well lasers $J_{th,\infty}$ is obtained. The extrapolated $J_{th,\infty}$ of 0.353 kA/cm^2 (0.176 kA/cm^2 per QW) is a rather good value for strained QW lasers emitting at 1.5 μm [16].

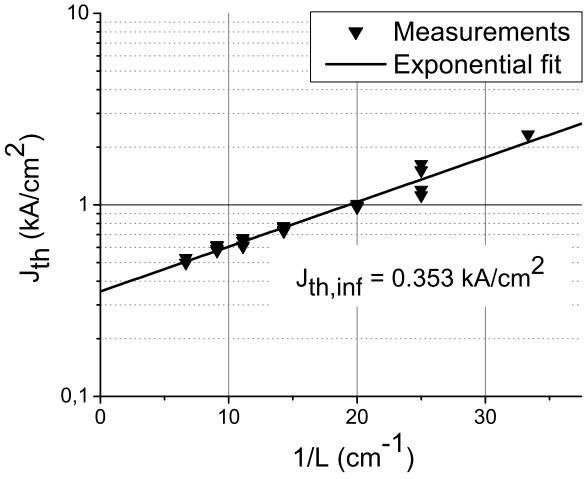

Figure 6.4: J_{th} vs $1/L$ for 5 μm wide lasers at 15^{o}C.

6.4 Characteristic Temperature

The threshold current temperature dependence is a function of several different parameters, most importantly the decrease in gain with temperature, discussed in section 4.4. It is usually approximated with an exponential function [6]

$$I_{th}(T) = I_0 e^{T/T_0} \tag{6.6}$$

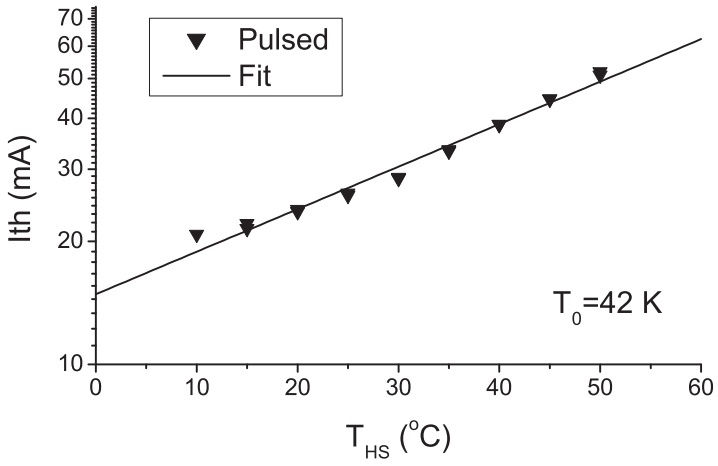

Figure 6.5: Threshold currents for different heatsink temperatures measured in pulsed mode fitted to equation 6.6.

where T_0 is the characteristic temperature of the laser. It is an important figure of merit for the lasers ability to work over a wide temperature range. The T_0 was fitted from pulsed mode measurements to 42 K for heatsink temperatures of 10^o-50^oC, seen in figure 6.5. This is in the lower range of observed values for the AlGaInAs material system, and low compared to many other material systems [6]. The reason for the low T_0 is probably the quaternary buffer materials in the barrier and SCH [17]. By reducing the SCH, a better T_0 would be expected.

6.5 Gain Properties

The empirical gain equation 4.32 can be fitted by using lasers with different length, relating the threshold current density and the net gain, which is clamped to the mirror losses at threshold, see figure 6.6. Losses from section 6.2 and the lateral diffusion width from section 6.1 was used for the fit.

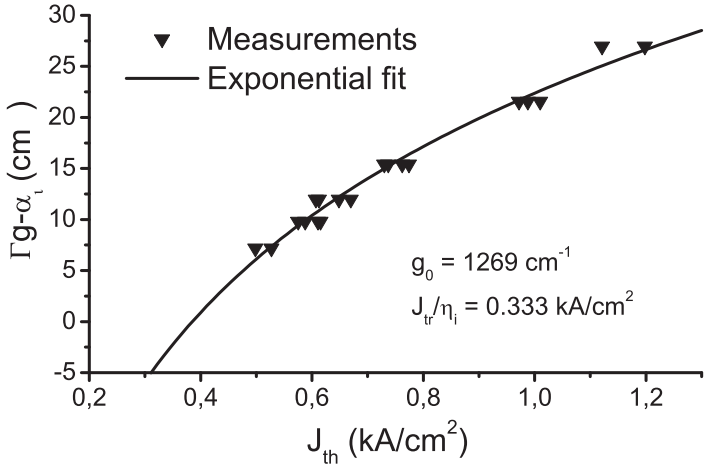

Figure 6.6: Net gain at threshold plotted against threshold current density for 5 µm wide lasers at 15^{o}C.

Hence, the parameters w_{diff}, η_i, α_i, g_0 and J_{tr} can be determined from the PI-measurements, see table 6.2.

w_{diff}	1.2 µm
α_i	1.7 cm^{-1}
η_i	62%
$J_{th,L=\infty}$	0.353 kA/cm^2
$J_{th,L=\infty}/N_{QW}$	0.176 kA/cm^2
T_0	42 K
g_0	1269 cm^{-1}
J_{tr}/η_i	0.333 kA/cm^2
J_{tr}	0.207 kA/cm^2
J_{tr}/N_{QW}	0.103 kA/cm^2

Table 6.2: Results from the PI-characterization of the MBE-grown active region, measured at 15^{o}C.

Chapter 7

Gain Spectra Measurement

The peak gain as a function of current density can be calculated from the P-I curves of lasers with different lengths, see figure 6.6. To measure the gain spectra a more elaborate method is required, such as the Hakki-Paoli method [1], described in section 2.3. This chapter will discuss the gain spectra measurements performed according to the Hakki-Paoli method. First the ASE-spectrum measurement and influence of the measurement equipment will be discussed. An extension to the Hakki-Paoli method proposed by Daniel T. Cassidy [18] to improve the accuracy will be described and later used to determine the net gain. The measurement procedure described in this chapter will be used in chapter 8 to characterize the gain properties of the active region.

7.1 ASE-Spectra Measurement

Using equation 2.19, the net gain spectrum can be calculated from the measured ASE-spectrum. This means that the accurate measurement of the gain spectrum is directly related to the accurate measurement of the ASE-spectrum. The ASE-spectrum was measured with an HP 70951B Optical Spectrum Analyzer (OSA). The lasers were mounted on a heatsink with a temperature controlled by a Peltier element. For a VCSEL, only the fundamental transversal TE mode is of interest. As the MCRW waveguide can support higher order transversal modes and also guide TM modes, see section 5.2, these modes must, if they exist, be filtered out in order to measure only the fundamental TE mode. In addition, the Hakki-Paoli method was derived considering only longitudinal modes and does not take higher order transversal modes or TM modes into account. Strictly speaking, the method actually requires a pure single transversal mode spectrum to work properly. Any influence from undesired modes must therefore be made as small as possible also for the gain spectra calculation to work.

In order to measure only the fundamental TE mode, a Polarization Maintaining (PM) fiber from Chiral Photonics with an in-fiber polarizer was used [19]. The fiber has a small aperture, of the same size as a single mode fiber, which filters out higher order transversal modes. The polarizer transforms the orthogonal linear polarizations to circular polarizations with different handedness. One of the circular polarizations is guided, while the other is scattered

out of the fiber core. By turning the fiber at the laser facet the TE or TM polarizations can be selected. However, no ASE-spectrum could be seen for the TM modes, meaning that the TM gain was very weak, as expected from the compressively strained quantum wells, see section 4.6. The polarizer has a specified extinction ratio exceeding 30 dB from 1525 nm to beyond 1600 nm, but an extinction ratio as large as 20 dB was observed already at 1510 nm. In addition, any higher order transversal modes or TM modes will have a different FSR than the fundamental TE mode, meaning that if they exist, they should be observed in the ASE spectra. No such modes were observed thanks to the small aperture PM fiber and in-fiber polarizer. It can thus be concluded that the measured ASE-spectrum was that of the fundamental transversal TE mode.

Any measurement performed is inevitably influenced by the measurement equipment and measurement technique used. In general every part of the measurement setup influences the signal to be measured in a non-ideal way. In the best case scenario, all or most of these deviations from the ideal setup does not have a significant influence on the measured property. The most important limitations influencing the ASE-spectra measurements and the subsequent gain spectra calculations will be described below. To aid the coming discussion, a measured ASE-spectrum from a 500 µm long MBE-grown MCRW laser can be seen in figure 7.1.

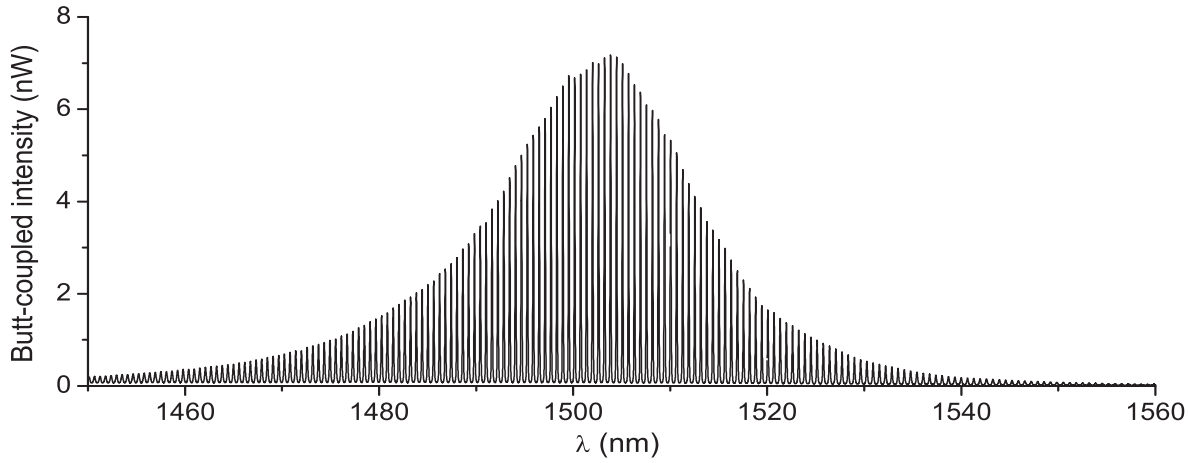

(a) Center of ASE-spectrum.

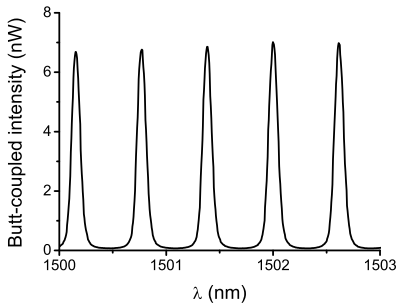

(b) Middle part of the above ASE-spectrum.

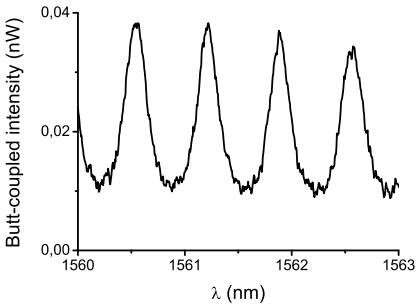

(c) Longer wavelength part of the above ASE-spectrum.

Figure 7.1: ASE-spectrum of a 500 µm long, 5 µm wide MCRW laser at 15^oC.

7.1.1 Optical Spectrum Analyzer Limited Linewidth

A problem when measuring optical spectra is the influence of the limited linewidth of the Optical Spectrum Analyzer (OSA). The measured spectrum will be a convolution between the true spectrum and the OSA response function. The influence of this can be compensated for by deconvolving the measured spectra with the OSA response function. The problem is that this response function is rarely known. It could potentially be measured by using the OSA to measure a laser with a well known linewidth, such as a Distributed FeedBack (DFB) laser.

To illustrate the effects of the limited OSA linewidth, a numerical example is seen in figure 7.2. The linewidth of the OSA is for this example taken to be a Gaussian with a FWHM of 0.1 nm since the OSA resolution bandwidth was 0.1 nm, see figure 7.2(b). A Fabry-Perot longitudinal mode, plotted with equation 2.9 is shown before and after convolution in figure 7.2(a).

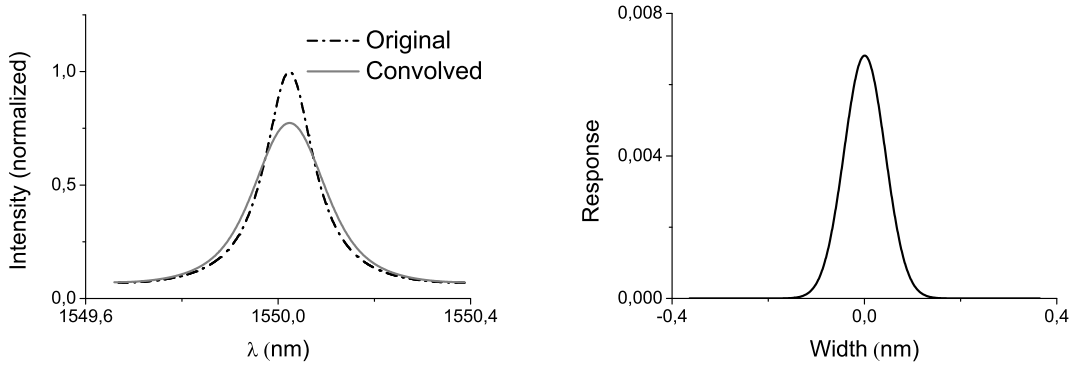

Figure 7.2: Simulated influence of the limited OSA linewidth. (a) One mode (one FSR) before and after convolution with the assumed Gaussian OSA response function seen in (b).

As seen, the influence of the OSA limited linewidth is to broaden the mode, as well as reduce its maximum. Since the OSA linewidth of 0.1 nm is similar to the Fabry-Perot mode FWHM, this effect will be important. It is important to note that the convolution conserves energy and merely redistributes the intensity in the spectral domain. The fact that the maxima gets lower and the minima slightly higher, will however lead to a too small max/min ratio ρ. The OSA limited linewidth will therefore lead to an underestimation of the gain when using the Hakki-Paoli method.

7.2 Cassidy's Extension to Hakki-Paoli

As discussed in the previous section, the limited linewidth of the OSA *redistributes* the intensity. To improve the accuracy, Daniel T. Cassidy proposed an improvement to the Hakki-Paoli method in 1984, where not the maximum/minimum ratio, but rather the average-mode-

intensity/minimum ratio [18] is used. Mathematically this is equivalent to the integration of equation 2.16 over one free spectral range. The integration yields [18]

$$I_{out,m} = \frac{I_{0,m}\left(1 + r_1 r_2 G_m\right)\left(1 - R_1\right)}{1 - \left(r_1 r_2 G_m\right)} \left(\frac{c}{2L}\right) \tag{7.1}$$

where the subscript m denotes the m^{th} longitudinal mode. By again forming the ratio P, this time between the average mode intensity and the adjacent minima, another quadratic equation in G_m is obtained. It can be solved for G_m as

$$\boxed{G_m = \frac{1}{r_1 r_2}\frac{P-1}{P+1} \qquad \rightarrow \qquad \Gamma g_m - \alpha_i = \frac{1}{L}\ln\left(\frac{P-1}{P+1}\right) + \frac{1}{L}\ln\left(\frac{1}{R}\right)} \tag{7.2}$$

A comparison of the Cassidy mode-sum/min and Hakki-Paoli max/min methods will now be performed by comparing the peak gain calculated from measured ASE-spectra.

7.3 Gain Specra Measurement

In reality the spectrum is equidistantly sampled by the OSA 2048 times per 10 nm interval (steps of less than 5 pm). All the measurement points between two minima are averaged to get the average mode intensity. As there is noise in the measured minima, the minimum value is also taken as an average over a few (10-20) measurement points between two peaks. A measured gain spectrum calculated from the ASE-spectrum in figure 7.1 with the mode-sum/min method can be seen in figure 7.3. The MATLAB function "'smooth"' is used to average the measured gain [20]. The function smooth uses a local regression of weighted linear least squares and a 2^{nd} degree polynomial.

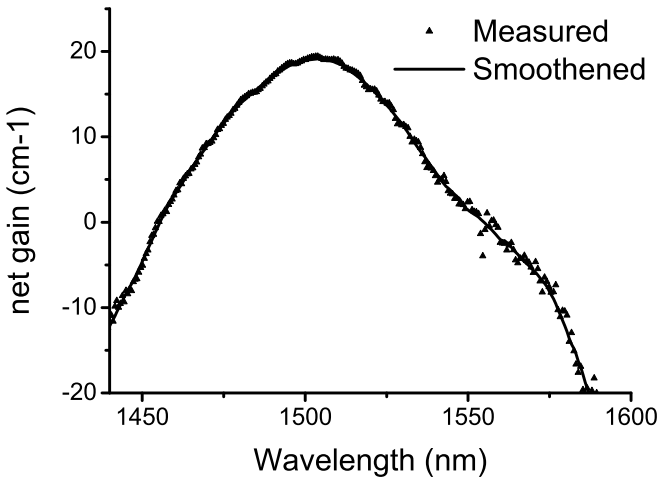

Figure 7.3: Gain spectrum measured with the Cassidy method.

The mode-sum/min method can now be compared to the max/min method. The accuracy of the mode-sum/min technique is found to be higher, as can be seen in figure 7.4. It measures a higher gain than the max/min method, with the measured maximum net gain clamping closer to, but still not at, the mirror losses. The reason for this is that the convolution with the OSA response function also increases the minima slightly, see figure 7.2. Neither of the two methods can correct this.

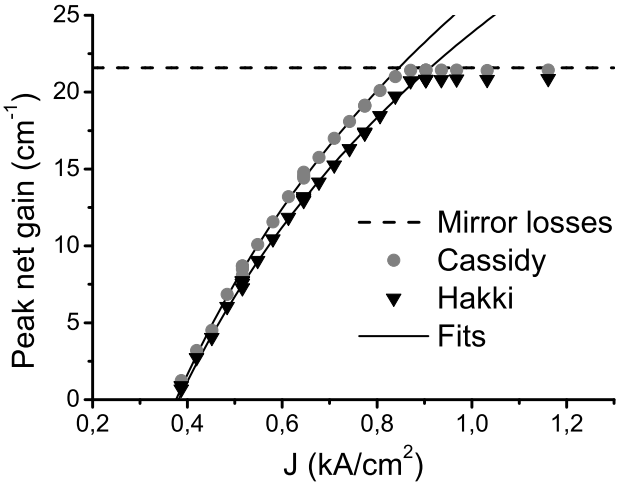

Figure 7.4: Peak gain as a function of current density using the Hakki-Paoli and the Cassidy method.

Both the measurement techniques in figure 7.4 were fitted using equation 4.32, yielding the parameters seen in table 7.1. The internal losses were taken from table 6.2 and the confinement factor from section 5.2.

	g_0 (cm^{-1})	J_{tr}/η_i (kA/cm^2)	peak net gain (cm^{-1})
max/min	1340	0.356	20.83
mode-sum/min	1441	0.353	21.43

Table 7.1: Paramters from the fits in figure 7.4. The net gain should be compared to the mirror losses $\alpha_m = 21.58\,\mathrm{cm}^{-1}$.

In conclusion, the mode-sum/min method calculates a higher and more accurate gain than the max/min method. The mode-sum/min method was therefore used in all gain spectra calculations in this work.

7.3.1 OSA Sensitivity

As the ASE-spectrum is measured below threshold, the output optical power is very low. The use of a small-aperture fiber to make sure that only the fundamental TE mode was measured further reduced the detected power. The low power means that the limited sensitivity of the OSA limits the detection. The signal-to-noise ratio will be especially low in the long-wavelength part of the ASE-spectrum, as the number of spontaneously emitted photons below

the bandgap is very low. In this range the difference between the maxima and minima of the measured spectra were as low as a few tens of picowatts, see figure 7.1(c). The impact of this will be described using figure 7.5.

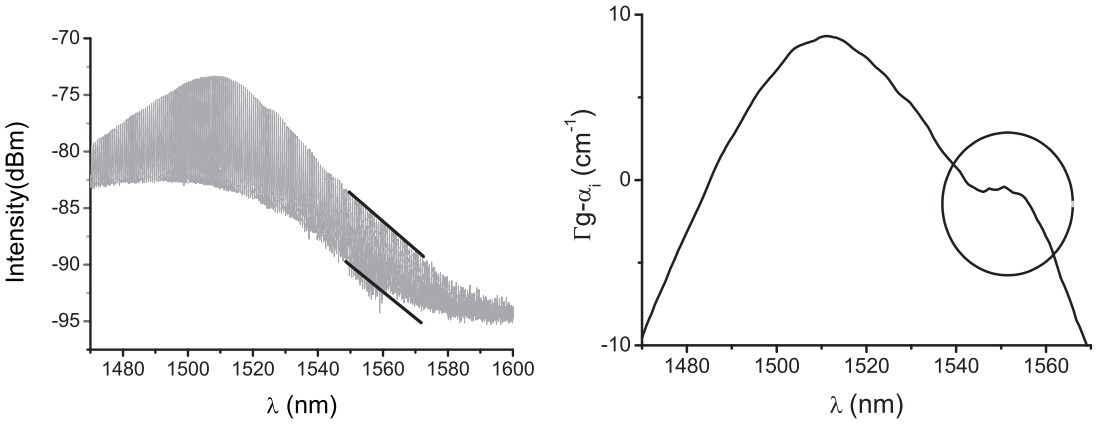

(a) Measured ASE spectrum.

(b) Gain spectrum.

Figure 7.5: Influence of noise.

Below the bandgap, the net gain spectrum should flatten out at a value equal to *minus* the internal losses α_i, which have been measured from the PI-curves to be 1.7 cm^{-1}. As seen from figure 7.5(b), the gain spectrum does briefly flatten out at approximately -1 cm^{-1} around 1550 nm. However, thereafter it plunges downwards with an unphysical increase in the optical losses. This is an effect of the small detected power and the OSA noise. For the gain to flatten out, the max-min ratio ρ has to be constant. When measuring the spectrum in dBm, this is equivalent to a constant difference between the maxima and minima, seen in figure 7.5(a). It can be seen that there is a fairly constant difference between the maxima and minima of about 8 dB from 1540 to 1555 nm, where the gain curve in figure 7.5(b) flattens out. After 1555 nm, the maxima keep decreasing, while the minima do not, see the black lines in figure 7.5(a). The minima have reached the noise floor due to the limited OSA sensitivity and can no longer be resolved, even with the averaging over 100 scans used to measure this ASE-spectrum. This results in a too small ratio ρ and a too small measured net gain, explaining the seemingly increasing losses at long wavelengths in figure 7.5(b).

The solution to this problem would be to increase the OSA sensitivity. This does however dramatically increase the OSA sweep time. To sweep time for a 5 nm wavelength span around 1580 nm is about 1.5 s when using a sensitivity of 2 pW, as used in figure 7.5. Using a sensitivity of 0.25 pW increases the sweep time more than 250 times to 400 s. This was nevertheless tested. The spectrum was observed using the higher sensitivity of 0.25 pW and averaging over 40 sweeps for long wavelengths, see figure 7.6.

By comparing this to figure 7.1(c) it is seen that it is possible to accurately resolve the spectrum for long wavelengths. It is even possible somewhat to resolve the spectrum around 1600 nm. As the OSA sweep time varies with detected power, measurement of the full spectrum takes roughly 30 hours. One such measurement was attempted, but since no cooling equipment could be left turned on overnight, the heatsink temperature, set by the lab room temperature, probably varied. Any small variation in the lab room temperature will make the

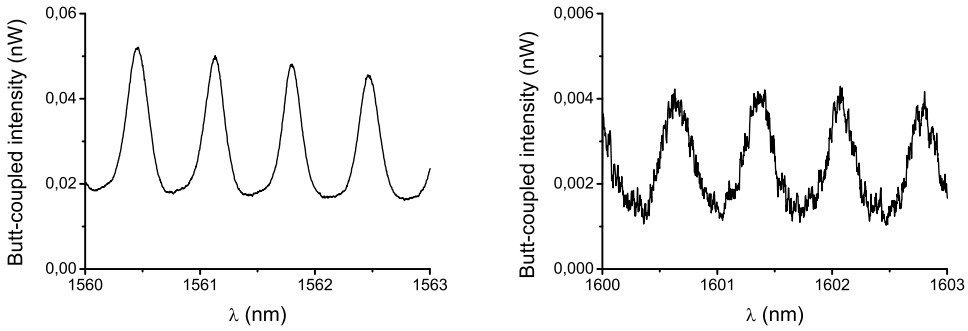

Figure 7.6: Demonstration of the improved signal-to-noise ratio obtained with extremely long integration times. Note the order of magnitude difference in the intensity scales between (a) and (b).

measurement unreliable. A stable heatsink temperature is needed, since even small temperature variations change the wavelengths of the modes as will be further discussed in section 8.1.2. If the modes shift while the OSA is averaging, the modes will be smeared out. This can be seen in the slight assymetric position of the minimas in figure 7.6(a). The lab room temperature can be expected to have changed during the integration time of 3-4 hours required for each 5 nm wavelength span in the long-wavelength part of the spectrum. Measuring ASE-spectra for several different currents and heatsink temperatures with integration times of up to 30 hours is of course not feasible. The gain spectra characteristics presented in the next chapter was therefore measured with an OSA sensitivity of 2 pW, at which the major part of the gain spectra still can be adequately resolved. The internal losses were taken from the PI measurements in section 6.2.

Chapter 8

Gain Spectra Characterization

This chapter will present the results of the gain spectra measurements on the MBE-grown active region. The measurement procedure was described in chapter 7. In order to have threshold currents similar to a VCSEL (ca. 1-2 kA/cm^2), a relatively short laser is necessary. The lasers showed good PI-characteristics down to lengths of 500 µm. On the basis of the PI-characterization, a 5 µm wide and 500 µm long laser was chosen for the gain spectra measurements. All results presented from now on were measured on that laser. The influence of the current density and the active region temperature on the gain was investigated.

8.1 Current Density Dependence

The gain spectrum was measured at constant heatsink temperature for different currents. This gives information about how different properties of the gain spectrum change with injected current density. However, the injected current has the secondary effect that it heats up the laser. This self-heating makes it impossible to measure the pure current density dependence of the gain spectra in CW mode, since different current densities will result in different active region temperatures. The solution to the problem would be to perform pulsed ASE-spectra measurements. Typical pulsed experiments on ridge waveguide lasers use a pulse length of 1 µs and 0.1% duty cycle [21]. This would reduce the average detected power by 30 dB, making pulsed measurement of the ASE-spectra very challenging due to the low signal-to-noise ratio, see section 7.3.1. Because of this, no pulsed gain spectra measurements were performed. CW spectra measurements to quantify the current density dependence of the gain spectra will still be meaningful if the self-heating causes a small effect compared to that caused directly by the current density. The self-heating must therefore be investigated.

8.1.1 Laser Self-heating

An MCRW laser has a power efficiency of roughly 10-20% depending on the bias point. The remaining 80-90% of the injected power is not converted into light, but dissipated as heat within the device. The dissipated power is

$$P_{diss}(I) = UI - P_{out}(I) \approx 1Volt * I \tag{8.1}$$

where U is the diode voltage, I the injected current and P_{out} the total output optical power (twice the output power measured from one facet). As a rule of thumb for quick thinking, the approximation in equation 8.1 can be used. It uses the fact that P_{out} is small compared to the total injected power UI and the voltage U is between 0.8-1.1 V for the laser, see figure 6.1. During CW operation the dissipated power will heat up the active region to a temperature

$$T_{act} = T_{HS} + \Delta T \tag{8.2}$$

where T_{HS} is the heatsink temperature and ΔT the heating caused by the dissipated power. This can be described with the thermal resistance of the laser R_T according to

$$\Delta T = R_T P_{diss}(I) \tag{8.3}$$

8.1.2 Thermal Resistance

The thermal resistance of the laser consists mainly of two series resistances. The heat generated inside the active region will first have to be conducted through the InP substrate which is ca. 150 µm thick after the wafer thinning. The heat will then flow through the backside contact and the epoxy glue bond to the heatsink. In general this problem is a two-dimensional heat conduction problem since the pumped active region width where the heat is generated is much smaller than the length, width and thickness of the laser chip. The thermal resistance from the substrate can be avoided by mounting the lasers upside-down on the heatsink [21], but this requires a different waveguide structure.

To initially get some idea about the magnitude of the thermal resistance, a formula for a two-dimensional heat flow from [6] was used,

$$R_T = \frac{\ln(4H/w)}{\pi \xi L} = 43K/W \tag{8.4}$$

where H is the height of the laser chip and $\xi = 68$ W/K/m [4] is the thermal conductivity of the InP substrate. Note that this only gives the thermal resistance of the laser chip, the epoxy glue bond is not included.

The temperature of the active region was also simulated using the finite element analysis software QuickField from Tera Analysis. The results from one simulation can be seen in figure 8.1. These simulations resulted in a thermal resistance of 53 K/W for the laser chip.

The thermal resistance can be measure by a number of different techniques. All methods consist of comparing CW and pulsed measurements to determine ΔT.

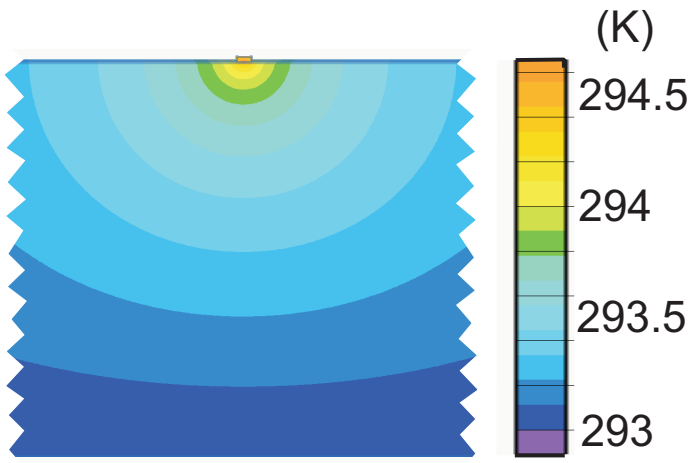

Figure 8.1: QuickField simulation of the self-heating in a laser chip at a current of 35 mA. The temperature of the QWs is 1.6^{o}C higher than the heatsink underneath the chip. Observe that the mesh continues on both sides and that the dark-blue line seen on the top of the chip is not a temperature indicator, but dark-blue lines showing the different material layers.

R_T from Fabry-Perot Spectrum

One of the most reliable methods to measure R_T is to observe the temperature-dependent wavelength shift of the Fabry-Perot longitudinal modes [22]. The laser is during the whole experiment biased at a constant current. The pulsed spectrum is observed and the wavelengths of four strong peaks are noted. A pulse width of 1 µs and a Duty Cycle (DC) of 0.1% is used for the measurement. The DC is then increased until it reaches 100% and the laser is operated in CW mode. The four peaks are tracked as they get red-shifted due to the increasing self-heating with a higher DC. Still operating the laser in CW mode, the self-heating ΔT is obtained as the decrease in heat-sink temperature necessary to blue-shift the four peaks back to the original pulsed wavelengths, see figure 8.2. The average of the four modes is used to calculate ΔT. By also noting the voltage and output optical power from a PI-measurement, the thermal resistance can be calculated according to equation 8.3. The results from four measurements performed under different conditions can be found in table 8.1.

T_{HS} (^{o}C)	I (mA)	ΔT (^{o}C)	$\partial\lambda/\partial T_{HS}$ (nm/K)	R_T (K/W)
15	30	2.2	0.128	72.7
15	50	2.4	0.143	59.2
30	50	2.7	0.121	58.8
30	70	4.4	0.132	73.7
average	-	-	0.131	66.1

Table 8.1: Results from the thermal resistance measurements on a 500 µm long 5 µm wide MCRW lasers.

The measured thermal resistance of ca. 70 K/W can be compared to calculated and simulated thermal resistance of the laser chip of 43 K/W and the 53 K/W respectively. This gives a thermal resistance of the epoxy glue bond of approximately 20-30 K/W, which is a reasonable

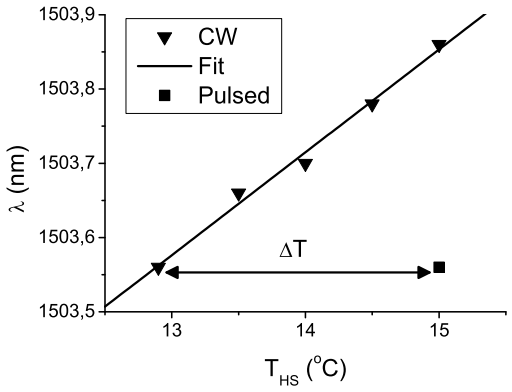

Figure 8.2: Determination of the self-heating by observing the wavelength of a single FP longitudinal mode in pulsed mode and the wavelength-shift with heatsink temperature in CW operation.

value. From the measurements it could be concluded that the self-heating at injected currents of 15-60 mA amounts to only ca. $1 - 4^o$C.

8.1.3 Current Dependence Measurements

Net gain spectra measured for several different currents can be seen in figure 8.3. It is notable how the gain clamps at threshold even though the Cassidy method is strictly speaking not valid above threshold. No higher order transitions were observed due to the finite band offsets as the conduction quantum well only has one subband, see figure 5.2. The gain for short wavelengths is seen to increase rapidly with increasing current, as the quasi-Fermi level separation increases, as expected from chapter 4. The expected decrease of the bandgap with injected current could not be observed due to the low signal-to-noise ratio for longer wavelengths, see section 7.3.1.

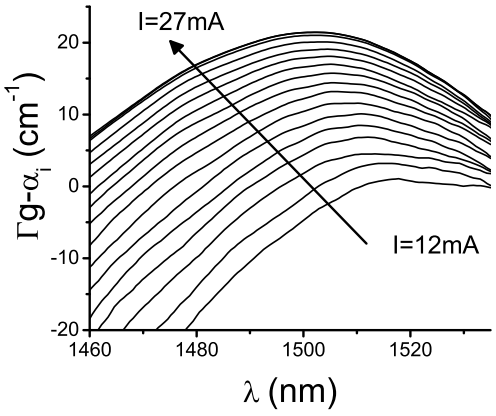

Figure 8.3: Net gain spectra measured at 15^oC in steps of 1 mA. Note that the gain clamps at $I_{th} = 26$ mA.

Similar measurements were done at several other heatsink temperatures. From these gain spectra, a number of different properties can be determined. The g_0 constant and J_{tr}/η_i are determined by fitting the peaks of the gain spectra against the injected current density using equation 4.32, see figure 8.4. Internal losses from the PI-measurements in section 6.2 and QW confinement factor from section 5.2 was used for the fit. Since the self-heating was found to be only a couple of degrees over the entire pumping range used in figure 8.4, it is possible to separate the direct influence of the different currents from the negligible secondary self-heating effect.

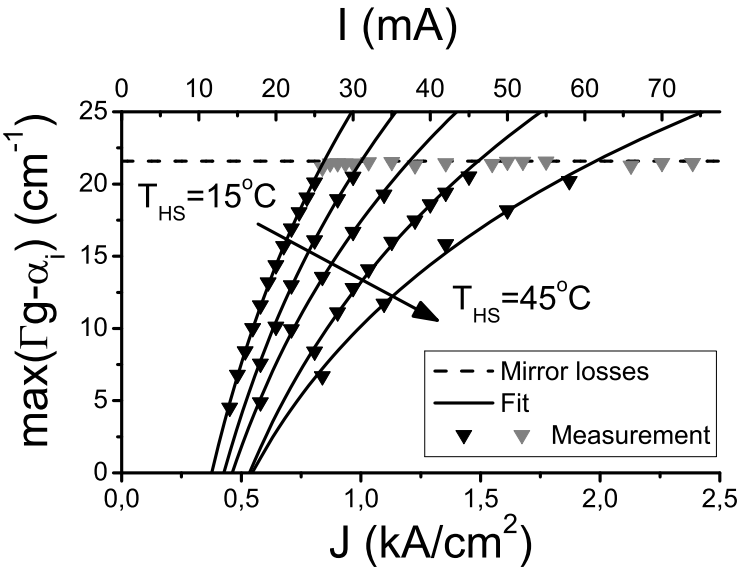

Figure 8.4: Peak net gain against current density and current measured at $T_{HS} = 15^o - 45^o$C in steps of 7.5^{o}C. Clamped points are shown in gray.

The fitted values can be seen in figure 8.5. It can be noted that the internal optical losses α_i only affects the fitted transparency current density and not g_0. Hence, even if a slightly wrong α_i is used, the g_0-plot in figure 8.5(a) is still valid.

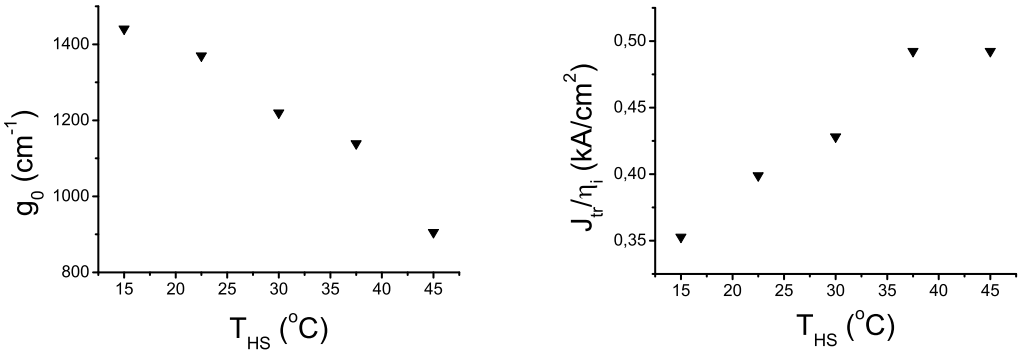

(a) (b)

Figure 8.5: Fitted values plotted against heatsink temperature.

The J_{tr}/η_i increases for higher temperatures, meaning that a larger current is needed to reach transparency, or in other words to separate the quasi-Fermi levels more than the bandgap according to the Bernard-Duraffourg condition. Also g_0 itself decreases with temperature as the gain is broadened and flattened due to a spreading of the occupation according to the Fermi-Dirac distribution for higher temperatures, see equation 4.11. This is reflected in the rather low $T_0 = 42$ K value measured for this laser, see section 6.4.

Further, the wavelength shift of the peak gain with current was found to have a linear behavior until clamping, see figure 8.6(a). The corresponding blue-shift rate until threshold in nm/mA was found to decrease linearly with temperature from 0.91 nm/mA for the peak gain at $T_{HS} = 15^o$C to 0.25 nm/mA at 45^o. The FWHM of the modal gain is shown in figure 8.6(b). As expected the FWHM of the modal gain increases with current and also with temperature until clamping.

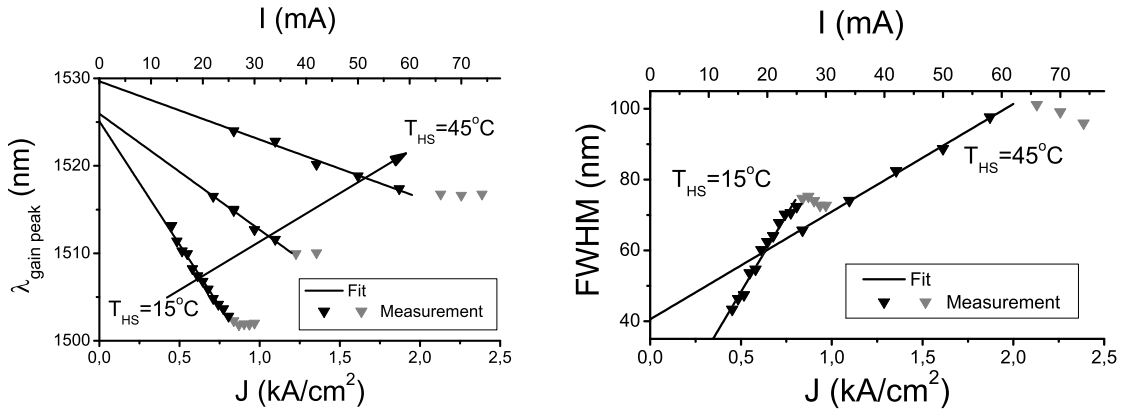

Figure 8.6: (a) Peak gain wavelength against current density measured at $T_{HS} = 15^o, 30^o$ and 45^oC. Clamped points are shown in gray. (b) Modal gain FWHM against current density measured at $T_{HS} = 15^o$ and 45^oC. Clamped points are shown in gray.

8.2 Gain Spectrum Temperature Dependence

The temperature dependence of the gain was investigated by measuring the gain at constant current density with varying the heatsink temperature. A rather low current of 26 mA was chosen to to be able to measure the gain spectra below threshold from $T_{HS} = 15^o - 45^o$C. The constant current will give rise to a constant self-heating of the active region, meaning that true active region temperature was $T_{HS} + \Delta T(I = 26mA) \approx T_{HS} + 1.8^o$C. The gain spectra for different T_{HS} can be seen in figure 8.7(a).

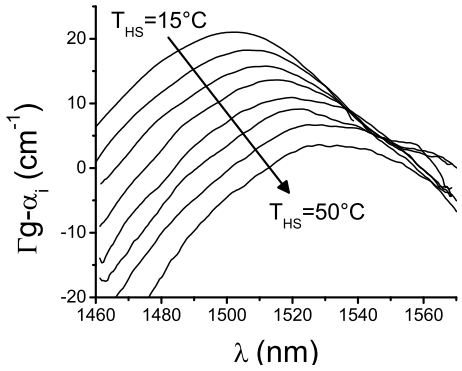

(a) Net gain spectra at $26mA$ for different heat sink temperatures in steps of 5^oC.

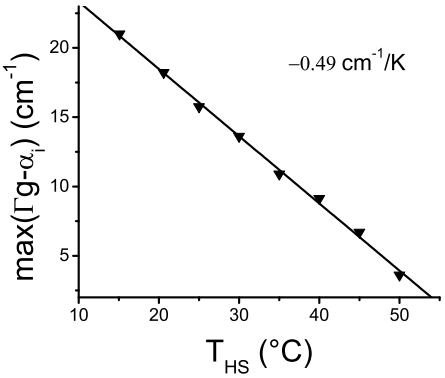

(b) Max net gain at $26mA$ for different heat sink temperatures.

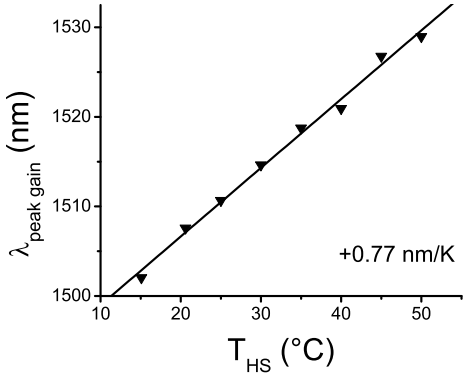

(c) Gain peak wavelength at $26mA$ for different heat sink temperatures.

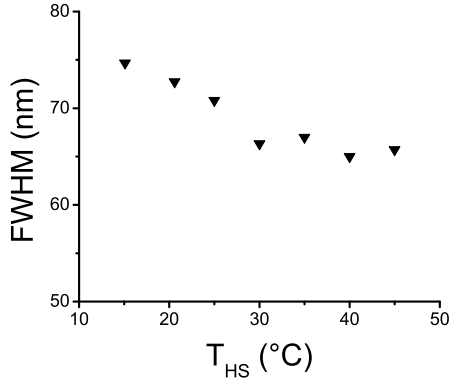

(d) Modal gain FWHM at $26mA$ for different heat sink temperatures.

Figure 8.7: Gain properties at constant current and different T_{HS}.

The peak net gain was found to decrease with 0.49 cm^{-1}/K. A very important property is the peak gain wavelength increase with temperature, which was found to be 0.77nm/K. This is crucial when considering the overlap between the gain and the DBR stopband to optimize the VCSEL for operation in a specific temperature range. The modal gain FWHM was found to be quite constant with temperature for constant current density.

8.3 Summary

All the measured values are summarized in table 8.2. The fitted g_0 and J_{tr}/η_i value obtained are slightly different for the PI and gain spectra measurements. This can be explained by that the values from the PI-measurement are fitted using several lasers of different lengths, see section 6.5, while the gain spectra measurements were performed on only one laser. To quantify the influence of the process tolerance on g_0 and J_{tr}/η_i, the gain spectra of more lasers would have to be measured.

PI-measurements	
w_{diff}	1.2 µm
α_i	1.7 cm^{-1}
η_i	62%
$J_{th,L=\infty}$	0.353 kA/cm^2
$J_{th,L=\infty}/N_{QW}$	0.176 kA/cm^2
T_0	42 K
g_0	1269 cm^{-1}
J_{tr}/η_i	0.333 kA/cm^2
J_{tr}	0.207 kA/cm^2
J_{tr}/N_{QW}	0.103 kA/cm^2
Gain spectra measurements	
R_T	66 K/W
$g_0(T_{HS} = 15^oC)$	1441 cm^{-1}
$g_0(T_{HS} = 45^oC)$	906 cm^{-1}
$J_{tr}/\eta_i(T_{HS} = 15^oC)$	0.353 kA/cm^2
$J_{tr}/\eta_i(T_{HS} = 45^oC)$	0.492 kA/cm^2
$\Delta\lambda_{peak}/\Delta I(T_{HS} = 15^oC)$	-0.91 nm/mA
$\Delta\lambda_{peak}/\Delta I(T_{HS} = 45^oC)$	-0.25 nm/mA
$FWHM(T_{HS} = 15^oC)$ at threshold	75 nm
$\Delta FWHM/\Delta I(T_{HS} = 15^oC)$	2.8 nm/mA
$FWHM(T_{HS} = 45^oC)$ at threshold	101 nm
$\Delta FWHM/\Delta I(T_{HS} = 45^oC)$	0.98 nm/mA
$\Delta g_{net}/\Delta T_{HS}$	-0.49 cm^{-1}/K
$\Delta\lambda_{peak}/\Delta T_{HS}$	0.77 nm/K

Table 8.2: Results from the PI and gain spectra characterization. The heatsink temperature is 15^oC unless otherwise noted.

Chapter 9

Conclusion

A process and measurement procedure for the characterization of active regions with the emphasis on the optical gain was developed during this master thesis. An MBE-grown two-QW active region emitting at 1.5 μm was characterized by PI and ASE-spectra measurements.

The process showed a high yield with reproducible results for lasers of equal width and cleaved length. The most important process step was the etching of the InP waveguide, where the etch depth was precisely controlled. Leaving a thin InP layer before the SCH grading layer was found to yield the best result. Internal losses of $\alpha_i = 1.7\,\mathrm{cm}^{-1}$ was fitted from PI-measurements, compared to the calculated material losses of $1.8\,\mathrm{cm}^{-1}$. It can therefore be concluded that the wet etch, designed to reduce waveguide losses, worked well. The lasers had threshold currents of 26 mA for 500 μm long lasers with 5 μm ridges. Due to the lack of lateral current confinement underneath the ridge, an effective lateral carrier diffusion width of 1.2 μm was measured for 5-10 μm wide ridges at 15^{o}C meaning that 20% of the injected current escapes the region underneath the ridge at threshold. This was shown to be in good agreement with a simple theoretical model.

By using 500 μm long lasers, the gain spectrum could be measured at current densities between 0.5-1.2 kA/cm^2 at 15^{o}C. As the laser had a low $T_0 = 42\,\mathrm{K}$, the current density at threshold increases rapidly with temperature.

The measured ASE-spectra contained no TM modes nor higher order transversal modes thanks the compressively strained quantum wells and the in-fiber polarizer and small-aperture fiber. Simply butt-coupling the fiber to the laser resulted in a low detected power, which limited the ability to resolve the minima in the long-wavelength part of the ASE-spectra. The internal losses could therefore not be determined from the ASE-spectrum in a good manner without the use of extremely long integration times. As expected, the Cassidy mode-sum/min method calculated a higher and more accurate gain from the ASE-spectrum than the Hakki-Paoli max/min method.

It was shown that the laser self-heating due to the injected current was small enough to be neglected, allowing gain spectra measurements to determine both the current density and temperature dependence of the gain spectrum. A g_0=1441 cm^{-1} and was fitted from the gain spectra measurements at 15^{o}C, decreasing to $906\,\mathrm{cm}^{-1}$ at 45^{o}C. Also the transparency

carrier density was seen to decrease with temperature. The peak gain was found to be blue-shifted until threshold at a rate of 0.91 nm/mA at 15^{o}C, with the rate decreasing linearly to 0.25 nm/mA at 45^{o}C. For increasing temperature the peak gain was red-shifted at a rate of 0.77 nm/K. Increasing the current density was found to increase the modal gain FWHM, while a temperature increase alone had no significant influence on the FWHM. A FWHM of 100 nm was observed at 45^{o}C, which should make this active region suitable for integration in a widely tunable MEMS-VCSEL.

This process and measurement method can now be employed to investigate the impact of new active region designs on the gain spectrum. Interesting investigations could for instance be the number of quantum wells, different strain and new materials. These measurements are also very interesting for a fixed wavelength VCSEL, since the overlap between the gain spectrum and DBR stopband has to be optimized for the required operating temperature range. An InGaAsP MOVPE-grown laser was also processed. It showed promising characteristics with a lower threshold current density than the MBE, due to a larger lateral diffusion width of 4.2 µm. Due to time limitations of a half-year thesis, no full characterization of this laser was made.

Bibliography

[1] B.W. Hakki, T.L. Paoli, *Gain spectra in GaAs double-heterostructure injection lasers*, J. Appl. Phys. vol.46 no.3 p.1299-1306, 1975

[2] European Technology Platform Photonics21, *Lighting the way ahead - Photonics21 Strategic Research Agenda*, Second edition, Germany, 2010

[3] Koyama et al., *Room temperature cw operation of GaAs vertical cavity surface emitting laser*, Trans. IEICE, E71(11) p.1089-1090, 1988

[4] W. Hofmann, *InP-based Long-Wavelength VCSELs and VCSEL Arrays for High-Speed Optical Communication*, Doctoral Thesis, Walter Schottky Institut, TU München, 2009

[5] *www.subtune.eu*, accessed 14^{th} May 2010

[6] L.A. Coldren, S.W. Corzine, *Diode Lasers and Photonic Integrated Circuits*, John Wiley & Sons, New York, 1995

[7] D.T. Cassidy, *Comparison of rate-equations and Fabry-Perot approaches to modeling a diode laser*, J. Appl. Opt. vol.22 p.3321-3326, 1983

[8] H. von Känel, *Energy-efficient lighting with semiconductors*, Lecture script, ETH Zurich, 2008

[9] C. Kittel, *Introduction to Solid State Physics*, 8^{th} edition, John Wiley & Sons, New Jersey, 2005

[10] A. Larsson, *Semiconductor Optoelectronics - Device Physics and Technologies*, lecture script, Chalmers University of Technology, 2009

[11] R. Soref, J. Lorenzo, *All-Silicon Active and Passive Guided-Wave Components for λ = 1.3 and 1.6 μm* , IEEE J. Quantum Electron. vol.22 no.6 p.873-879, 1986

[12] M.-C. Amann, B. Stegmueller, *Calculation of the effective refractive-index step for the metal-cladded-ridge-waveguide laser*, J. Appl. Opt. vol.20 no.8 p.1483-1486, 1981

[13] T. Ikegami, *Reflectivity of Mode at Facet and Oscillation Mode in Double-Heterostructure Injection Lasers*, IEEE J. Quantum Electron. vol.8 no.6 p.470-476, 1972

[14] G.J. Letal et al, *Determination of Active-Region Leakage Currents in Ridge-Waveguide Strained-Layer Quantum-Well Lasers by Varying the Ridge Width*, IEEE J. Quantum Electron. vol.34 no.3 p.512-518 1998

[15] K. Shinoda, A. Taike, H. Sato, H. Uchiyama, *Highly Reliable InGaAsP/InP Lasers with Defect-Free Regrowth Interfaces Formed by Newly Composed HBr-Based Solutions*, 13^{th} International Conference on InP and Related Materials, Japan, 2001

[16] P. Thijs et al, *Progress in Long-Wavelength Strained-Layer InGaAs(P) Quantum-Well Semiconductor Lasers and Amplifiers*, IEEE J. Quantum Electron. vol.30 no.2 p.477-499, 1994

[17] B. Stegmueller, *Low Threshold Current MOVPE Grown GaInAs-Al(Ga)InAs Separate Confinement Heterostructure Multiquantum Well Metal-Clad Ridge-Waveguide Lasers Emitting at 1585 nm*, IEEE Photon. Tech. Lett. vol.2 no.9 p.609-611, 1990

[18] D.T. Cassidy, *Technique for measurement of the gain spectra of semiconductor diode lasers*, J. Appl. Phys. vol.56 no.11 p.3096-3099 1984

[19] Chiral Photonics, *http://www.chiralphotonics.com/*, accessed 22^{th} May 2010

[20] MATLAB help, *smooth*, MATLAB version 7.10.0.499 (R2010a)

[21] M. Kubota et al, *Thermal Properties of 1.3 μm AlGaInAs Multi Quantum Well Ridge Waveguide Lasers*, Jpn. J. of Appl. Phys. vol.39 p.2297-2300, 2000

[22] T.L. Paoli, *A New Technique for Measuring the Thermal Impedance of Junction Lasers*, IEEE J. Quantum Electron. vol.11 p.498-503, 1975

Appendix A

Nomenclature

Abbreviations

ASE	Amplified Spontaneous Emission
CW	Continuous Wave
DBR	Distributed Bragg Reflector
DC	Duty Cycle, Direct Current
DFB	Distributed FeedBack
ECR	Electron Cyclotrone Resonance
FP	Fabry-Perot
FSR	Free Spectral Range
FTTH	Fiber To The Home
FWHM	Full-Width at Half Maximum
HDTV	High-Definition TV
HH	Heavy Hole
IPTV	Internet Protocol TV
LASER	Ligth Amplification by Stimulated Emission of Radiation
LH	Light Hole
MBE	Molecular Beam Epitaxy
MCRW	Metal-Clad Ridge-Waveguide
MEMS	Micro-Electro-Mechanical System
MOVPE	MetalOrganic Vapor Phase Epitaxy
OSA	Optical Spectrum Analyzer
PM	Polarization Maintaining
QW	Quantum Well
RIE	Reactive Ion Etch
SCH	Separate Confinement Heterostructure
TE	Transverse Electric
TM	Transverse Magnetic
UHV	Ultra-High Vacuum
VCSEL	Vertical-Cavity Surface-Emitting Laser
VoD	Video on Demand
WDM	Wavelength Division Multiplexing
WSI	Walter Schottky Institut

Latin symbols

$\mathbf{A}$	vector potential
B	magnetic field
c	speed of light
D_{eff}	effective diffusion coefficient
d	active region thickness
E	energy, electric field
F	envelope function
f	Fermi-Dirac distribution
G	linear gain
g	exponential gain
H	laser chip height, Hamiltonian, Heaviside's step function
h	Planck's constant
$\hbar$	reduced Planck's constant
I	intensity, current
J	current density
j	imaginary unit
k	wavevector
k_B	Boltzmann's constant
L	laser length
M_T	transition matrix element
m	particle mass, also used as index
N	density of states
n	refractive index
P	power, mode-sum/min ratio
p	hole density
$\mathbf{p}$	momentum operator
q	elementary charge
R	(power) reflectance, resistance,

	transition rate
r	(amplitude) reflectivity
$\mathbf{r}$	position vector
T	temperature
U	voltage
u	Bloch function
w	ridge width

Greek symbols

α	optical losses
β	wavevector
Γ	confinement facor
δ	Dirac's delta function
η	efficiency
θ	optical phase
λ	wavelength
ν	frequency
ρ	max/min ratio
τ	carrier lifetime
ψ	wavefunction
ω	angular frequency

Subscripts

0	vacuum, free-space
C	conduction band
$diff$	diffusion
F	Fermi
g	group
HS	heatsink
i	internal
m	mirror
T	thermal
th	threshold
V	valence band

Superscripts

$*$	effective
$\rightarrow$	propagation direction

Appendix B

Epitaxial Layers

MBE-Edge Emitter **(M4599)** AlGaInAs @ 1.55µm

Layer	Material	E_G (eV) / λ_G (µm)	x_{Al}	y_{Ga}	d (nm)	$\Delta a_{rel}/a$	*n*-doping	*p*-doping	µ (cm²/Vs)	ρ (Ωcm)	α_{fc} (cm^{-1})	α_{IVBA}(cm^{-1})	$\alpha_{tot.}$(cm^{-1})	*n* (@1.55)	$n_{corr.}$	Γ (%)
n-Clad	InP:Si	1,353 / 0,916	0	0	500	0,0E+00	8E+17		2200	3,5E-03	2,3	0	2,3	3,166	3,162	2,9
	InP:Si	1,353 / 0,916	0	0	120	0,0E+00	5E+17		2500	5,0E-03	1,3	0	1,3	3,166	3,164	4
n-SCH1	AlGaInAs:Si	1,128 / 1,099	0,2744	0,2030	20	-4,5E-04	5E+17		3900	3,2E-03	1,3	0	1,3	3,333	3,330	1,1
	AlGaInAs	1,128 / 1,099	0,2744	0,2030	350	-4,5E-04					0,0	0	0,0	3,333	3,333	40
QW	AlGaInAs	0,722 / 1,717	0,0870	0,2031	6	1,2E-02					0,0	0	0,0	3,511	3,511	0,923
Barrier	AlGaInAs	1,128 / 1,099	0,2744	0,2030	7	-4,5E-04					0,0	0	0,0	3,333	3,333	1,1
QW	AlGaInAs	0,722 / 1,717	0,0870	0,2031	6	1,2E-02					0,0	0	0,0	3,511	3,511	0,924
p-SCH1	AlGaInAs	1,128 / 1,099	0,2744	0,2030	350	-4,5E-04					0,0	0	0,0	3,333	3,333	41
	AlGaInAs:C	1,128 / 1,099	0,2744	0,2030	20	-4,5E-04		5E+17	160	7,6E-02	0,1	13	12,7	3,333	3,332	1,1
p-Clad	AlInAs:C	1,437 / 0,863	0,4747	0,0000	30	8,4E-06		5E+17	20	6,2E-01	0,6	11	11,6	3,200	3,198	1,4
	InP:Be	1,353 / 0,916	0	0	90	0,0E+00		5E+17	72	1,4E-01	0,2	15	15,2	3,166	3,165	2,8
	InP:Be	1,353 / 0,916	0	0	1380	0,0E+00		1E+18	72	8,6E-02	0,4	30	30,4	3,166	3,164	3,2
Contact	GaInAs:C	0,734 / 1,690	0	0,4656	50	1,5E-06		4E+19	59	7,9E-03	42,0	1200	1242,0	3,811	3,721	0

$\alpha_{Sum.}$(cm^{-1})	**1,8**

Appendix C

Process Sheet

Edge Emitter – MCRW Laser

Start date:

Finishing date:

Sample No.:	Comment:

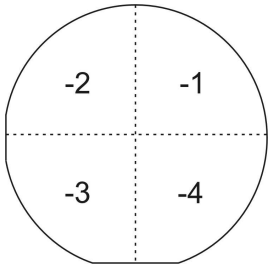

Masks:

- Lat. Laser 1.1:

  Width of stripes (μm):

  1 30 10 7 5 4 3 30 10 7 5 4 3 2

- Lat. Laser 1.2:

  Saw-tooth step = 50 μm

- Randweg

MBE Edge Emitter (M4599) AlGaInAs @ 1.55μm

Layer	Material	E_G (eV) / E_G (eV)	x_{Al}	y_{Ga}	d (nm)	$\Delta a_{rel}/a$	n-doping	p-doping	μ (cm^2/Vs)	ρ (Ωcm)
n-Clad	InP:Si	1.353 / 0.916	0	0	500	0.0E+00	8E+17		2200	3.5E-03
	InP:Si	1.353 / 0.916	0	0	120	0.0E+00	5E+17		2500	5.0E-03
n-SCH1	AlGaInAs:Si	1.128 / 1.099	0.2744	0.2030	20	-4.5E-04	5E+17		3900	3.2E-03
	AlGaInAs	1.128 / 1.099	0.2744	0.2030	350	-4.5E-04				
QW	AlGaInAs	0.722 / 1.717	0.0870	0.2031	6	1.2E-02				
Barrier	AlGaInAs	1.128 / 1.099	0.2744	0.2030	7	-4.5E-04				
QW	AlGaInAs	0.722 / 1.717	0.0870	0.2031	6	1.2E-02				
p-SCH1	AlGaInAs	1.128 / 1.099	0.2744	0.2030	350	-4.5E-04				
	AlGaInAs:C	1.128 / 1.099	0.2744	0.2030	20	-4.5E-04		5E+17	160	7.6E-02
p-Clad	AlInAs:C	1.437 / 0.863	0.4747	0.0000	30	8.4E-06		5E+17	20	6.2E-01
	InP:Be	1.353 / 0.916	0	0	90	0.0E+00		5E+17	72	1.4E-01
	InP:Be	1.353 / 0.916	0	0	1380	0.0E+00		1E+18	72	8.6E-02
contact	GaInAs:C	0.734 / 1.690	0	0.4656	50	1.5E-06		4E+19	59	7.9E-03

Start hotplate for lithography ☐

Sample cleaning ☐

1-2 min warm acetone (ca. 150 ^{o}C)

1-2 min warm propanol

Use sample cleaning cups with rocks

HCl dip ☐

Important to improve resist sticking!

30 s $HCl:H_2O = 1:4$

Dry 120 s on hotplate at same temperature as the resist spin-on

Ridge definition ☐ (Negative process, ∼1.7 μm resist thickness)

∼40 s nitrogen gun blowing

Resist **AZ5214** spread out

Resist spin-on **Prg. 4 (3000 U/min)**

Baking of resist **90 s 90 ^{o}C** Hotplate

∼10 min cool down

Silvered side on the metal when installing the mask!

Edge (if needed backside) exposure ☐ **and Edge development** ☐
60 s **18 mW/cm^2** Developer **AZ400K:H_2O = 1:4**
Standard time: **30 s**

Mesa exposure ☐ Mask: **Lat. Laser 1.1** (Align in the middle of the circles)

2.2 s **18 mW/cm^2**

Image-Reversal ☐

30 s	**125^{o}C**	Hotplate
10min		cool down
22 s	**18mW/cm^2**	Flood-exposure

Mesa development ☐ Developer **AZ400K:H_2O = 1:4**

Expected development time: ∼**11 s +** ∼**5 s** (Use two glasses with developer)

Sample	Real time (s)	Resist thickness (∼1,7 μm)

Check development in the lithography-room microscope ☐

Barrel etcher ☐

(Removes approx. 50-100 nm photoresist)
5 min 250 sccm O_2 / 200 W (Prg. 16)

Optional: Microscope pictures ☐

Ridge etching, passivation and contact-window opening

Wet etch in case of Al-rich capping layers ☐

$HBr:H_2O_2:H_2O$ = 10:1:30 = 20ml:2ml:60ml

Work under suction!

Stir and wait for ∼10 min until red-orange-colored

Use 2 water baths

Don't swing while etching!

Etch rate ca 30nm/s

Warning: Etch rate is strongly spatially varying

ECR (methane etch, layer 5) ☐

Insert dummies! ☐ **Also good for preventing the sample from being blown of the carrier!**
Does not etch Al-rich layers
Resist burns if etched too long in one step! (Maximal safe time tried: ∼15 min)
Etch rate @ 15 min etch: ∼25 nm/min (Resist:∼12nm/min)
Etch ca 3x15 min to etch ∼1um

- Turn on gasses
- Condition with Si-carrier for ca 20 min
- Load sample and pump down for ca 15 min **(Dummies!)**
  - Etch
  - Unload sample and cool in vented load lock for 5 min, repeat!

Run cleaning program afterwards (57 min) ☐
Shut off microwave, turn of gasses ☐

Wet etch to smoothen etch roughness ☐

$HBr:Br_2:H_2O$ = 150:1:1800

Work under suction!

Stir with magnetic fish until the Br_2 is dissolved

Use 2 water baths

Don't swing while etching!

Etch rates InP∼40nm/min, GaInAsP∼25nm/min

Sample:			
Resist (nm)	Process no	Etch t (s)	Etch depth (nm)

Sample:			
Resist (nm)	Process no	Etch t (s)	Etch depth (nm)

Sample:			
Resist (nm)	Process no	Etch t (s)	Etch depth (nm)

Sample:			
Resist (nm)	Process no	Etch t (s)	Etch depth (nm)

Optional: Microscope pictures ☐

If no wet etch step was done:
HCl dip just before sputtering ☐ HCl:H_2O = 1:5, 30 s

SiO_2-Sputtering ☐ Process-nr.:_____
Insert dummy! ☐

Dummy:	Ultrasonic bath (30%) 5 min	
Targeted thickness:	150nm	True thickness: __________
	600V, ~50 min (Rate can fluctuate!)	
	SiO_2 deposition rate: ~3.3 nm/min	Deposition rate: __________

Optional: Microscope pictures ☐

Lift-off ☐ (sample must at all times be covered with acetone or propanol)

Do not let sample soak in acetone before ultrasonic bath! Pieces of SiO_2 may stick on the sample!

- Ultrasonic bath (10%): 5 min (cold acetone)
- Ultrasonic bath (10%): 5 min (cold acetone)
- Cold-warm acetone: 3 min (**submerge the sample in cold acetone and warm it!**)
- warm propanol: 3 min

(Warm = 150^{o}C)

Dektak measurement ☐

With program #4 (no lackmessung!)

Sample	Thickness (nm)	Etch depth (nm)

Optional: Microscope pictures ☐

Thermal anneal in case of MOVPE sample ☐

To activate the Zn dopants.

Use the oven in the cleaving room.

Sandwich samples, ie put the first sample down and the other upside down on top of the first one. Thus having both the samples etched surfaces lying in contact.

Anneal 10 min @ 420^{o}C in N_2 atmosphere.

Separate Lasers ☐ (Negative process, ∼1.7 μm resist thickness)

∼40 s nitrogen gun blowing

Important on SiO_2: HMDS adhesion promoter. Spin-on and nitrogen blowing ☐

Resist **AZ5214** spread out

Resist spin-on **Prg. 4 (3000 U/min)**

Baking of resist **90 s 90 ^{o}C** Hotplate

∼10 min cool down

Silvered side on the metal when installing the mask!

Edge (if needed backside) exposure ☐ **and Edge development** ☐
60 s **18 mW/cm^2** Developer **AZ400K:H_2O = 1:4**
Standard time: **30 s**

Mesa exposure ☐ Mask: **Lat. Laser 1.2** (Adjustment: 2 crosses, check the mesas)

2.2 s **18 mW/cm^2**

Image-Reversal ☐

30 s	**125^{o}C**	Hotplate
10min		cool down
22 s	**18mW/cm^2**	Flood-exposure

Mesa development ☐ Developer **AZ400K:H_2O = 1:4**

Expected development time: **∼11 s + ∼5 s** (Use two glasses with developer)

Sample	Real time (s)	Resist thickness (∼1,7 μm)

Check development in the lithography-room microscope ☐

Barrel etcher ☐

(Removes approx. 50-100 nm photoresist)
5 min 250 sccm O_2 / 200 W (Prg. 16)

Optional: Microscope pictures ☐

VT 118: Ti/Pt/Au-Top-contact

Open nitrogen (30 min before) ☐

HCl-Dip & ventilate air-lock ☐

Mixture HCl:H_2O = **1:4** 20 s

Vapor deposition VT 118 ☐ Ti / Pt / Au $\sim$ 300 / 800 / 3000 Å

Rotate sample @ 30^o during deposition.

Optional: Microscope pictures ☐

Lift-off ☐(sample must at all times be covered with acetone or propanol)

cold acetone	2-3 min (15 min if necessary)
Ultrasonic bath (10%):	1 min (cold acetone)
Cold-warm acetone	3 min (**submerge the sample in cold acetone and warm it!**)
warm propanol	2 min

(Warm = 150^{o}C)

Collect the gold with a tissue over the drain.

Optional: Microscope pictures ☐

Wafer thinning ☐target ca. 150 μm

- Bond sample (Heat to 150^o to melt glue)
  - Carefully push down to remove air bubbles
  - Squeeze together using the metal weight with 3 filter papers on top
- Grinding
  - Measure sample thickness before starting
  - Use AlO 3 μm grains, rotation at 50 and 2 small metal weights on top
  - Add water to reduce thinning rate
  - Thin wafer for $\sim$1-3 min, measure thickness, iterate!
- Sample cleaning
  - Clean away dirt from the holder before sliding off the sample! Or sample will scratch!
  - Remove from metal holder (150^o or slightly more)
  - Clean in two glasses (acetone and propanol) with a filter paper in each

(Throw all dirty papers in special waste bin)

Sample	Thickness (μm)

n-backside contact metallization (n-Anlage)

Dip before evaporation ☐

$HCl:H_2O$ = 1:4 20 s

Be very careful!!!!! Don't swing the sample!!!!

n-Anlage vapour deposition ☐ Ge / Au / Ni / Au = 130 / 330 / 100 / 3000 Å

Control if the option "Schiffchenheizung gewählt ist" -> Green light on "the bucket" not on "the lying ladder"!

Be very careful with the mounting needles!

Pitch: **0**^{o}

Thermal anneal of Ge/Au/Ni/Au contacts ☐

Warning: The oven in the cleaving room overshoots 60-70^{o}C in the first 10s. Use 300^{o}C instead!

Choose one of the following:

- 1 min @ 360^o in N_2 atmosphere ☐
- 1 min @ 300^o in N_2 atmosphere @ 20 mbar in cleaving room RTA ☐

Turn off the N_2 gas afterwards